Experiments on the drag of a flat plate moving parallel to an air-water interface

Naren Balaji Vijayaragavan

Technische Universiteit Delft

Experiments on the drag of a flat plate moving parallel to an air-water interface

by

Naren Balaji Vijayaragavan

in partial fulfillment of the requirements for the degree of

Master of Science
in Mechanical Engineering

at the Delft University of Technology,
to be defended on Wednesday January 31, 2018 at 02:00 PM.

P & E Report Number : 2876

Supervisors:	Dr. ir. M.J. Tummers	TU Delft
	ir. E.J Grift	TU Delft
Thesis committee:	Prof. dr. ir. J. Westerweel,	TU Delft
	Dr. ir. B.W. van Oudheusden,	TU Delft

TU Delft Delft University of Technology

Acknowledgments

I would like to thank my supervisors *Dr. Mark Tummers* and *Ir. Ernst Jan Grift* for giving me this amazing opportunity. This work would never have been possible without their encouragement and guidance. Thank you *Ernst Jan* for your trust, patience and assistance. I can't thank you enough.

I would like to express my gratitude to *Prof. Jerry Westerweel* and *Dr. B.W. van Oudheusden* for being a part of my thesis committee.

I am also extremely grateful to the support staff at the Laboratory for Aero and Hydrodynamics. *Jasper Ruijgrok*: Thank you for fabricating the model for me with great attention to detail. *Jan Graafland*: Thank you for your help with all the necessary equipment to build my hydrogen bubble visualization setup. *Edwin Overmars*: Thank you for helping me with the PIV setup and for providing me with an amazing high speed camera.

A special thanks goes out to my friend *Sai Krishna* for his help and support. I would like to thank my friends *Veera, Adi, Vaibhav and Keerthi* for their enjoyable company.

Finally, my deepest thanks are due to my parents and friends in India. Thank you for your love and support throughout.

Naren Balaji
Delft, January 2018.

Abstract

Rowing is a competitive sport where victory is determined by fine margins. In the past, the focus has been on optimizing the shell. Due to the increasing regulations placed on the shell design, the scope for manoeuvring in this area is greatly limited. This increases the necessity to focus on the less explored option of propulsion in rowing. The propulsion is caused by the momentum transfer from the rowers to the water with the help of oar blades. The design of these oar blades has also been extensively studied. However, knowledge on the effect of the air-water interface on the drag force on the oar blades is still lacking. Therefore, visualizing the flow around the oar blades will lead to better understanding of the flow structures, which would help in optimizing the drag force acting on the oar blades.

In the present study, a simplified scenario of a rectangular flat plate moving normally to its plane along a straight line and parallel to the free surface has been studied using hydrogen bubble visualization and Particle Image Velocimetry (PIV). Using a 4-axes industrial robot and a force/torque transducer, the effect of the air-water interface on the drag force on the plate has been studied at a Reynolds number, based on the longest edge of the plate, of 6×10^4. The analysis of the drag force profiles at different plate depths led to the identification of a high drag case, which occurred at a plate depth h of 20 mm. The hydrogen bubble visualization indicated that in this specific case, the high drag was related to the formation of a compact wake behind the plate.

Hydrogen bubble visualizations were also performed at two other plate depths, $h = 0$ and $h =$ 100 mm, to determine the effect of the air-water interface on the flow structures and ultimately on the drag force acting on the plate. The visualization of the deep water case ($h =$ 100 mm) captured the formation of a vortex ring, which was found to have unique effects on the drag force. The presence of the air-water interface was found to significantly influence the drag force on the plate. Additionally, an extensive decomposition of the drag force profile showed a time-dependent added mass force and a decaying force acting on the plate.

Particle Image Velocimetry (PIV) measurements were carried out in the horizontal mid-plane of the plate. The tracking of the starting vortex and its disintegration has been identified using the swirling strength analysis. Finally, combining the hydrogen bubble visualization and PIV results, the formation and the development of the starting vortex was identified.

Contents

Acknowledgment iii

Abstract v

1 Introduction 1
- 1.1 Background of the investigation . . . 1
  - 1.1.1 How does rowing work? . . . 1
  - 1.1.2 Drive or recovery? Propulsion or drag? . . . 1
  - 1.1.3 What happens during the drive phase? . . . 2
- 1.2 Simplification of the scenario . . . 3
- 1.3 Review of previous works . . . 3
  - 1.3.1 Influence of acceleration . . . 4
  - 1.3.2 Presence of a free surface . . . 5
  - 1.3.3 Sharp edges and vibrations of the flat plate . . . 6
  - 1.3.4 Vortex formation . . . 6
- 1.4 Objectives . . . 7
- 1.5 Outline of the report . . . 8

2 Experimental setup 9
- 2.1 Main setup . . . 9
  - 2.1.1 Tank and robot . . . 9
  - 2.1.2 Flat plate . . . 10
- 2.2 Sensors and data acquisition . . . 10
- 2.3 Hydrogen bubble visualization setup . . . 12
  - 2.3.1 Test matrix for hydrogen bubble visualization . . . 14
- 2.4 PIV setup . . . 14

3 Results and disucssion 17
- 3.1 Torque/force on the flat plate . . . 17
- 3.2 Basic decomposition of the force on the plate . . . 18
- 3.3 Effect of the plate depth on the drag force . . . 19
- 3.4 Effect of the air-water interface . . . 21
  - 3.4.1 Overview of the base case (h = 100 mm) . . . 21
  - 3.4.2 Differences between the base case (h = 100 mm . . . 23
- 3.5 Extensive decomposition of the drag force profile . . . 27
  - 3.5.1 Drag force decomposition . . . 28
  - 3.5.2 Modelling the acceleration phase . . . 29
  - 3.5.3 Physical significance of the forces F_{AM} and F_{DECAY} . . . 33
- 3.6 Vortex shedding frequencies . . . 33

3.7 Particle Image Velocimetry 36
3.7.1 Setup parameters 37
3.7.2 Comparison with hydrogen bubble visualization results 38
3.7.3 Tracking the starting vortex 40
3.7.4 Total circulation in the measurement plane 42

4 Conclusions **45**

Bibliography **47**

A Effect of hydrogen bubble visualization on drag force measurement **49**

B Stitching the velocity fields to obtain the desired field of view **53**

1

INTRODUCTION

Rowing is a sport based on propelling a boat with the help of oar blades. As a competitive sport, performance enhancement is of the utmost importance. This can be achieved either by physical improvement of the rower to generate a greater force or through a technological innovation of the rowing system. The possibility of improving the race time through modifications of the rowing system, rather than physically burdening the rower is worth looking into. This section summarizes the elements constituting rowing, leading to the area of interest of the current work.

1.1 BACKGROUND OF THE INVESTIGATION

1.1.1 How does rowing work?

During rowing, the boat is propelled by the transfer of momentum from the rowers to the water. This transfer occurs in two ways: motion of the oar blade with respect to the water and movement of the rower with respect to the boat. These activities take place during the rowing stroke. During this stroke, the *catch* is the moment when the oar blade is placed in the water and *extraction* is when the oar blade is removed from the water. Hence, the rowing stroke can be split into two distinct parts, *catch to extraction* known as the *drive phase* and *extraction to catch* known as the *recovery phase.* During the drive phase, the oar blade enters the water behind the rower, and is moved towards the stern along a circular segment as seen by an observer on the boat. At the end of the drive phase, the oar blade is removed from the water. From the extraction to the catch, the oar blade is taken back to the initial position (behind the rower) above water. This cycle of movements propels the boat forwards.

1.1.2 Drive or recovery? Propulsion or drag?

The physics of the drive and the recovery can be understood by studying the key forces involved during the rowing stroke. Figure 1 indicates these forces, namely gravity F_{GT}, buoyancy F_{BU}, drag F_D and propulsion F_B. Gravitational and Buoyancy forces determine the vertical equilibrium position of the boat. Drag forces depend on the frontal area of the boat shell, drag coefficient of the system, and the velocity of the boat with respect to water (Baudouin et al. [2002]). The propulsive force driving the system is generated by the rower using the oar blades. Baudouin et al. [2002] concluded that rowing performance can be improved by either increasing the propulsive force or by decreasing the drag on the boat, throughout the rowing stroke. The design of the rowing shell (Scragg et al. [1993]) and the hydrodynamics of the rowing boat have been extensively studied (Mola et al. [2006], Zhang et al. [2011], Day et al. [2011], Formaggia et al. [2008a], Formaggia et al. [2008b]), and the International Rowing Federation (FISA) poses certain guidelines on the boat design (FISA Rule Book, [2017]). Therefore, we are interested in the less explored option of improving the propulsion, during the drive phase, which involves optimizing the drag on the oar blade to improve efficiency.

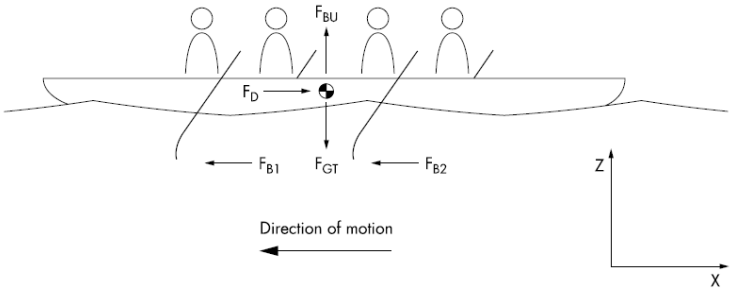

Fig. 1. Free body diagram of a boat-oar-rower system (Baudouin et al. [2002]).

1.1.3 What happens during the drive phase?

As discussed earlier, during the drive phase the movement of the oar blades through the water provides propulsion. Considering the relative motion of the boat in addition to the movement of the blade in water, the path traversed by the oar blade during the drive phase resembles a complex prolate cycloid motion, as seen in Fig. 2(a). It also shows that the longitudinal motion of the blade with respect to the boat motion is small compared to the latitudinal motion, as shown in Fig. 2(b). Thus, the oar blade is essentially locked in a pocket of water (Sliasas et al. [2009]). During this motion, vortices are shed from the blade through α (where α is the angle between the oar and the boat), as shown in Fig. 3. The presence of these vortices affects the lift and drag coefficients (Pulman [2005]) and the interaction of previously shed vortices with the oar blade makes it complex to investigate. He proposed that further research is necessary to understand the effects of hydrodynamic drag and lift forces upon acceleration.

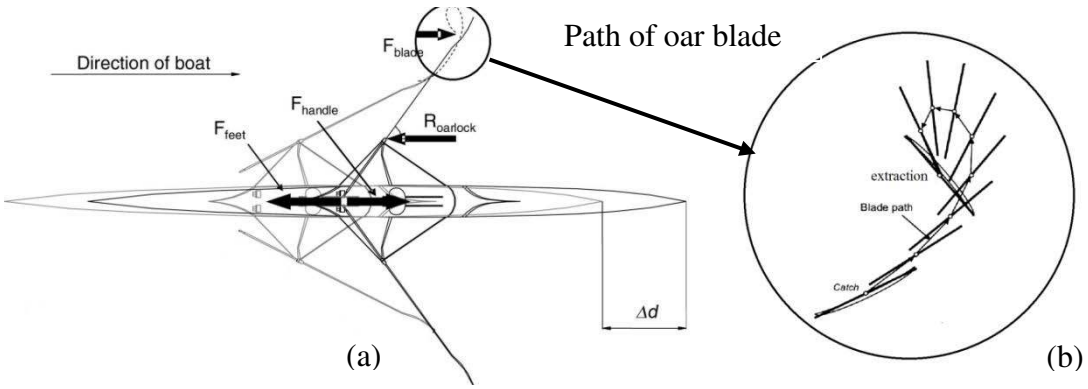

Fig. 2. (a) Overhead view of a single scull showing the forces that occur during the drive phase of the stroke. The single scull is shown at two instants with a movement Δd and the measured path (- -) of the centre of the oar blade is shown for a starboard oar (Kleshnev [1999]), (b) Path of blade center through water during the drive phase (Sliasas et al. [2009]).

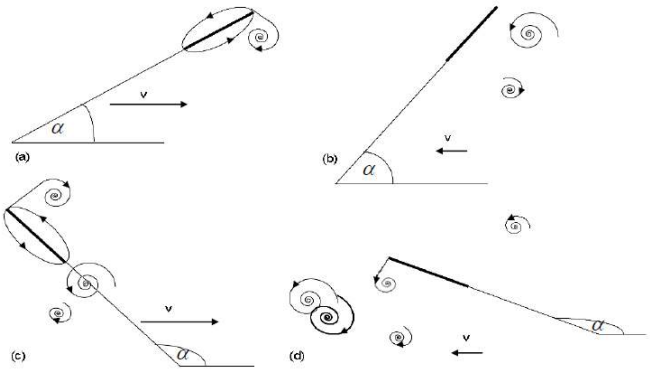

Fig. 3. Vortex formation through the drive phase of rowing stroke (Pulman [2005]).

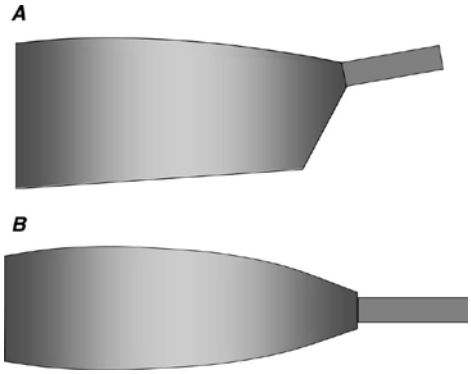

Fig. 4. Frontal views of Big Blade (A) and Macon (B) oar blade designs (Caplan et al. [2007b]).

1.2 SIMPLIFICATION OF THE SCENARIO

Ideally, the focus of the current work should be a hydrodynamic study of an oar blade following the complex path shown in Fig. 2. Lift force, F_L, and drag force, F_D, acting on the oar blade, which traverses along a path resembling a complex prolate cycloid, vary with time. F_L and F_D are defined as:

$$F_L = \frac{1}{2} \mathrm{C_L} \rho A V^2$$

and

$$F_D = \frac{1}{2} \mathrm{C_D} \rho A V^2,$$

where ρ is the fluid density, A is the surface area of the oar blade, and V is the relative velocity between the oar blade and water. $\mathrm{C_L}$ and $\mathrm{C_D}$ are the dimensionless lift and drag coefficients that are dependent on the oar blade shape and the angle of attack (Caplan et al. [2007a]).

However, the unsteady, three-dimensional flow around the oar blade in the vicinity of the air-water interface is a complex problem. Hence, it was decided to first study a relatively simple case where, the motion of the oar blade is along a straight line, shifting the focus to the presence of a free surface and the dynamic loading on the oar blade.

The lift and drag forces vary slightly between different blades like the Big Blade and the Macon that are shown in Fig. 4 (Caplan et al. [2007b]). Coppel et al. [2009] studied the hydrodynamic behavior of rowing oar blades using computational fluid dynamics (CFD). Their simulation of a Big Blade and a flat rectangular oar blade showed similar trends in lift and drag coefficients with different angle of attack. Because of this, it was decided to start with the simplest oar design, i.e. a rectangular flat plate. Essentially, this reduces the investigation to a study of hydrodynamics of a flat plate moving perpendicular to its plane along a straight line, close to the air-water interface.

1.3 REVIEW OF PREVIOUS WORKS

Research on the flow over flat plates moving perpendicular to its plane suggest that the flow is affected by factors like sharp/rounded edges of the flat plate, acceleration and vibrations of the flat plate and the presence of a free surface. This section provides a review of some works relating to these factors.

1.3.1 Influence of acceleration

One of the earlier works on the flow around a flat plate that moves perpendicular to its plane through water was performed by Taneda et al. [1971]. The work focused on a thin plate started either impulsively or with uniform acceleration. They visualized the flow using aluminium dust and electrolysis method at a low Reynolds number of 896, as shown in Fig. 5. As a result, they were able to determine the onset of separation of the flow at the edges and derived a relation between the length of the wake bubble with respect to acceleration, time and plate length.

Tonui et al. [2011] focused on the early stages of the flow around impulsively started objects. By using particle image velocimetry, they captured the temporal development of recirculation zones and primary eddies, as shown in Fig. 6.

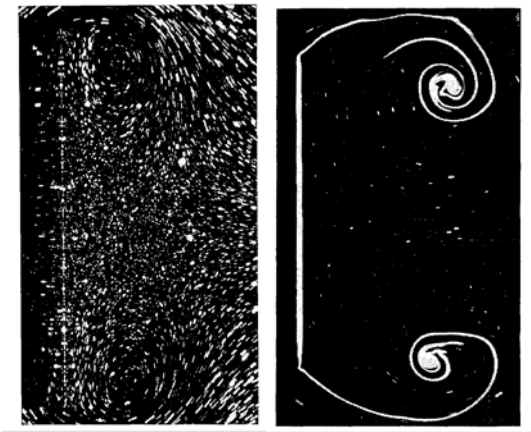

Fig. 5. Visualization of flow over flat plate, using aluminium dust (left image) and electrolysis method (right image) (Taneda et al. [1971]).

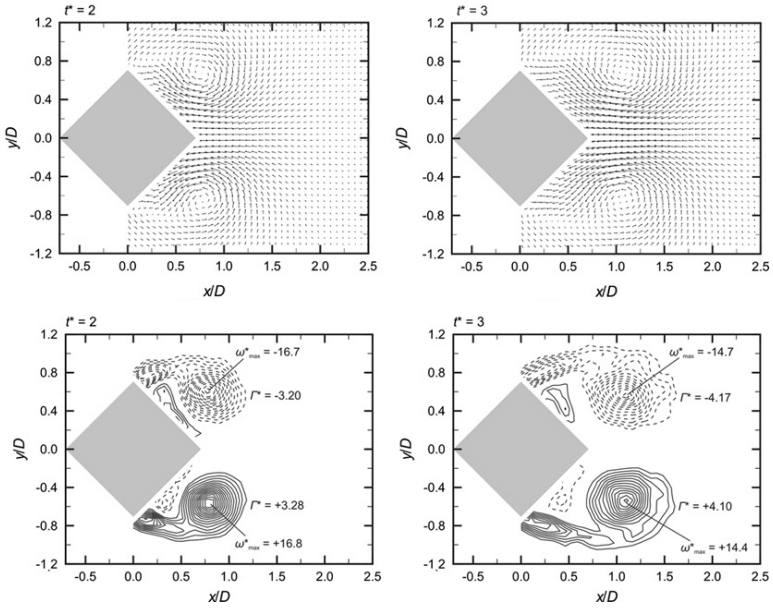

Fig. 6. Sequential snapshots of the velocity field (top) and vorticity field (bottom) for an impulsively started square prism (Tonui et al. [2011]).

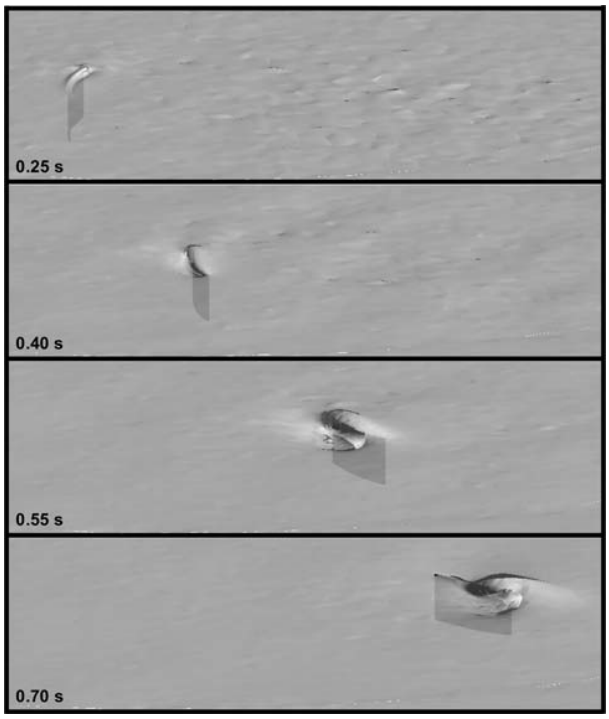

Fig. 7. Evolution of the free surface during the rowing stroke. Near the end of the stroke there is a surface bulge of approximately 10 cm above the blade and a depression of 8 cm behind the blade (Sliasas et al. [2009]).

1.3.2 Presence of a free surface

Sliasas et al. [2009] created a CFD model accounting for the interaction of a rectangular flat plate with the free surface of water. The outcome of the simulations were qualitatively similar to what was observed in the real rowing conditions, in terms of the general surface behaviour, quantifying the surface bulge in front of the oar blade and depression behind the blade, as shown in Fig. 7.

Leroyer et al. [2008] verified the capabilities of a RANS solver to compute the flow around an oar blade and to estimate the hydrodynamic forces. They studied an oar blade close to the free surface and the solver was capable of determining the deformations of the free surface, as shown in Fig. 8. The work was supported by experimental data on hydrodynamic forces acting on the oar blade, but lacked data on experimental visualization. Also, the effect of the depth of the oar blade below the free surface was not addressed.

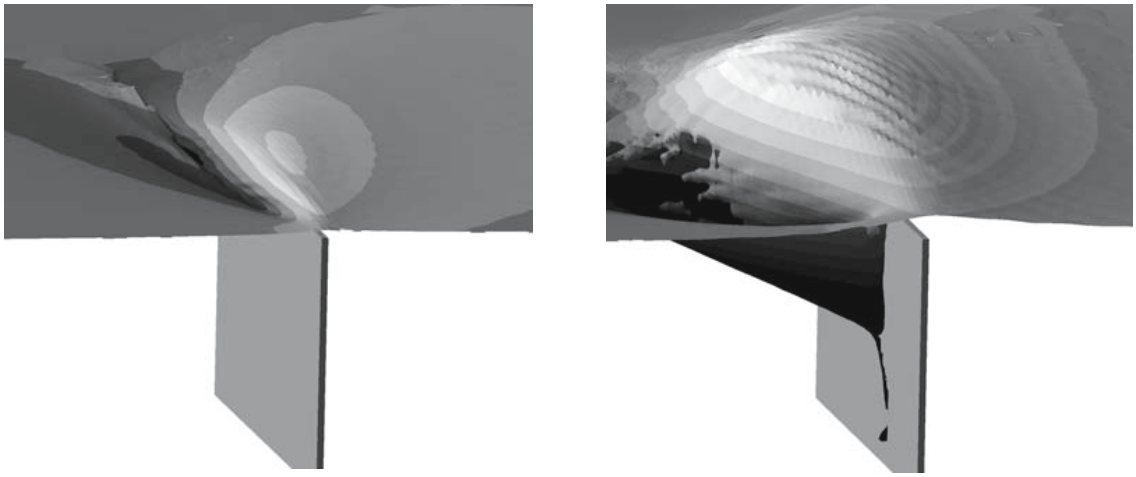

Fig. 8. Free surface deformations (Leroyer et al. [2008]).

1.3.3 Sharp edges and vibrations of the flat plate

A major characteristic that was observed when studying the flow normal to the flat plate was a low-frequency unsteadiness which was observed in the work by Tian et al. [2014]. They studied the effects of sharp and smooth corners in a flat plate, at a high Reynolds number of 1.5×10^5 using large eddy simulations, as shown in Fig. 9. Their results showed a low frequency unsteadiness in the flow patterns and the flow switched between high and low drag regimes. They concluded that the sharpness of the corners of the plate increased the frequency of this switch and also increased the mean drag coefficient and the fluctuations in lift and drag coefficients.

1.3.4 Vortex formation

Gharib et al. [2011] worked on drag-based paddling propulsion, like in a paddle steamer, by rotating a flat plate immersed in water through an angle ϕ, as shown in Fig. 10. They studied the vortex formation and thrust performance using particle image velocimetry. Figure 11 shows a sketch of the vortex structures formed along the edges of the flat plate and the shedding of the tip vortices. Though the trajectory of the flat plate is not in a straight line, this work gives an idea about the vortex structures formed along the edges of the flat plate.

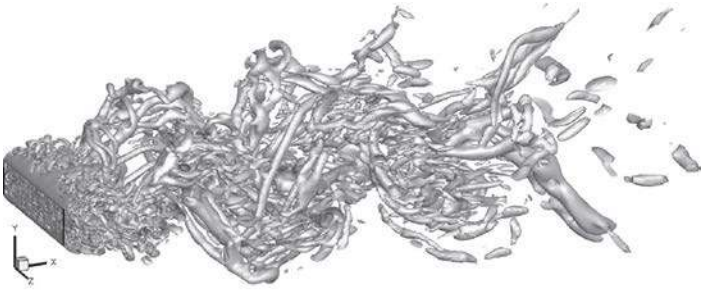

Fig. 9. Overall 3-D view of Q-criterion instantaneous iso-surfaces (Tian et al. [2014]).

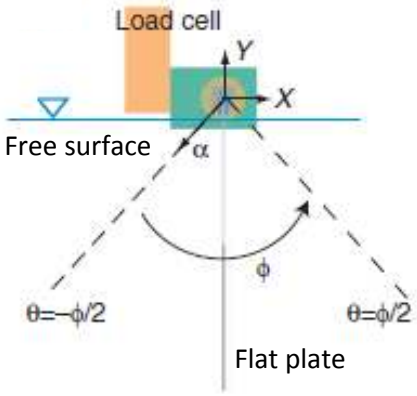

Fig. 10. Schematic of the paddling model used by Gharib et al. [2011] for rotation of the flat plate.

Fig. 11. Vortex formation process depicted using iso-surfaces of vorticity magnitude. The arrows in the first time step show the rotating direction of the vortex. T.V. indicates the position of the tip vortex (Gharib et al. [2011]).

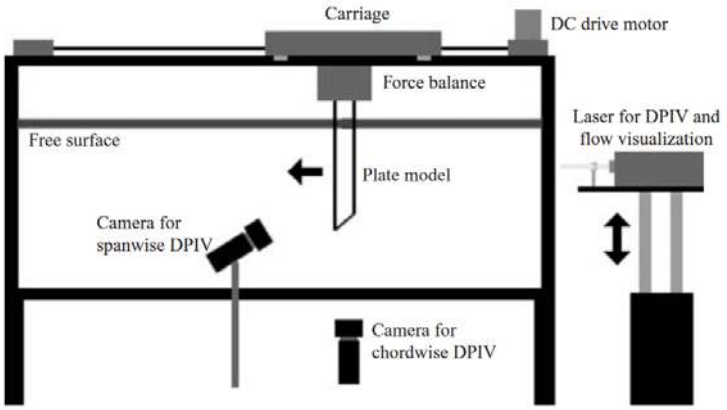

Fig. 12. Schematic of the towing tank and DPIV hardware used by Ringuette et al. [2007].

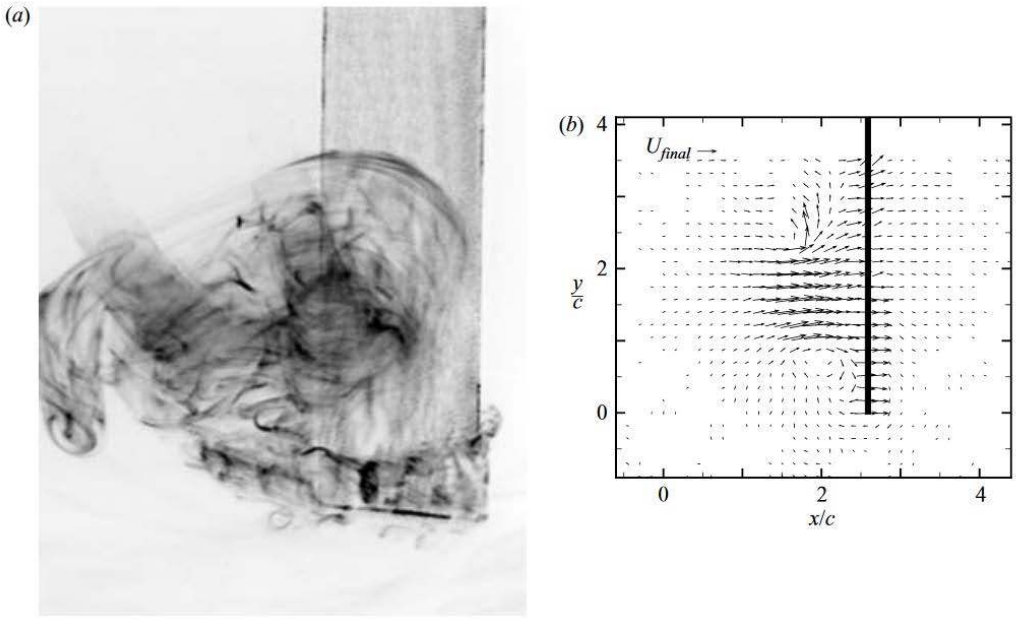

Fig. 13. (a) Three-dimensional dye visualization at the free end of the flat plate, (b) Velocity field from PIV in a vertical plane parallel to the flow (Ringuette et al. [2007]).

Ringuette et al. [2007] considered a rectangular flat plate undergoing a translating motion in a towing tank at a Reynolds number 3.0×10^3, as shown in Fig. 12. They studied the role of the tip vortex, formed at the free end of the flat plate, on the force generated on the flat plates. They determined the chordwise and spanwise vorticity fields behind the flat plate using PIV. By performing trials with different plate aspect ratios below the free surface and utilizing dye visualization and PIV, as shown in Fig. 13, they were able to envision the formation and development of a large tip vortex and the leading edge vortices. They concluded that the tip vortex contributes substantially to the overall force on the plate. It should be noted that in this work, the flat plate was not entirely submerged in water.

1.4 OBJECTIVES

Considering the fact that the motion of a true rowing blade through the water is very complex, it was decided to consider a much simpler case of a rectangular flat plate moving along a straight line normal to its surface and parallel to the air-water interface. In this case, the flat plate experiences drag only (no lift) so that its relevance to rowing is limited to the start of a rowing race when the boat speed is still low. Despite the drastic simplification, the flow around the flat plate that moves along a straight line (normal to its surface) is still complex

due to its unsteady nature and the vicinity of the air-water interface. The main objectives of this research are:

i. To get a better understanding of the phenomena that occur in the flow around the plate and their contributions to the drag.
ii. To determine how these phenomena (and the drag) are affected by the presence of the air-water interface.

To achieve these objectives, an experimental investigation will be carried out in which the flat plate will be traversed (at various depths) through water in a precisely controlled manner by using an industrial robot arm. A force/torque transducer that connects the robot arm and the plate will be used to measure the drag. The flow around the plate will be visualized by using the hydrogen bubble technique, while Particle Image Velocimetry will be used to get more quantitative information about the velocity fields.

1.5 OUTLINE OF THE REPORT

The experimental setup of the current work is discussed in Chapter 2. This includes details on the test tank setup, sensors and data acquisition equipment. The setup used for hydrogen bubble visualization and Particle Image Velocimetry are discussed in some detail. Chapter 3 presents and discusses the results of the current work, followed by the conclusions drawn from it, in Chapter 4.

2

EXPERIMENTAL SETUP

The experiments were performed at the Row Bot lab facility in the Laboratory for Aero and Hydrodynamics of TU Delft. The facility includes an open top water tank and a 4-axes industrial robot. A hydrogen bubble visualization setup consisting of an electrical power source, electrodes and a high speed camera was used for visualizing the flow. A high-speed Particle Image Velocimetry (PIV) system was used to measure the velocity field in a planar cross section of the flow. In this chapter, the setup used is described in detail.

2.1 MAIN SETUP

2.1.1 Tank and robot

The current work requires linear translation of a flat plate through water. The setup consists of a glass tank with internal dimensions of 1.96 m length, 1.96 m width and 0.6 m depth, as seen in Fig. 14. The glass walls and the bottom of the tank provide full optical access, which makes it suitable for optical measurement techniques.

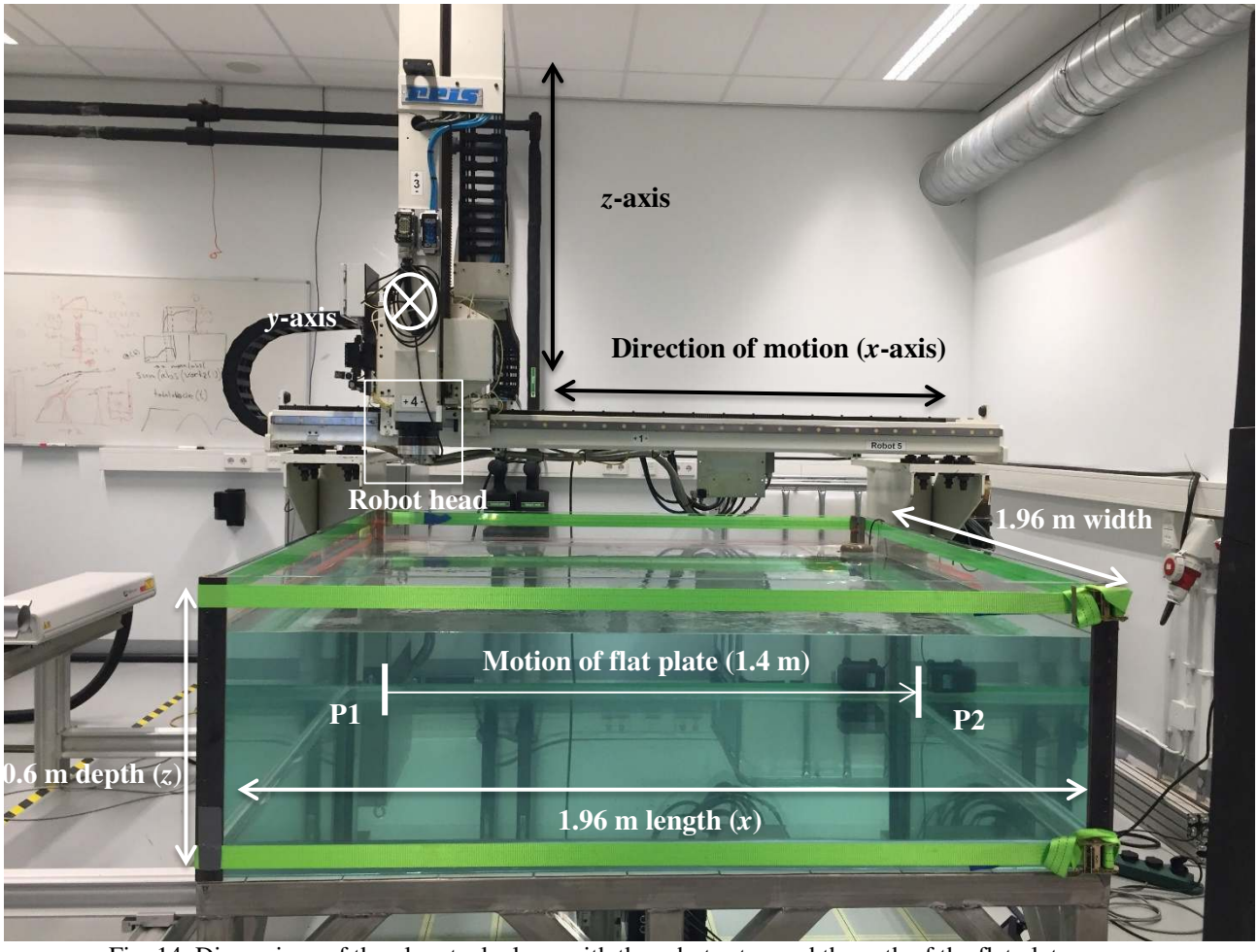

Fig. 14. Dimensions of the glass tank along with the robot setup and the path of the flat plate.

The tank is filled with water up to the level of 500 mm measured from the bottom of the tank. The laboratory is maintained at a temperature of 21 ºC ± 0.5 ºC. To facilitate motion of the flat plate through the water, a 4-axes RL50 Reis robot is used to move the flat plate through the water in a prescribed manner. The robot head can reach a maximum speed of 2.8 m/s along the x and y-axes, and 1.8 m/s along the z-axis. The robot head can also rotate about the z-axis. The positioning of the robot head has a repeatability of ±0.1 mm. The default acceleration of the robot head is 0.82 m/s^2. This default is defined as 100% robot acceleration. Robot acceleration can be manually set between 0-200%, which corresponds to 0-1.64 m/s^2. The servo control is connected to the Reis ROBOTstarV robot control, which allows free motion controls and also programmable motion controls through a portable teach pendant. This system is also connected to a PC via Ethernet, allowing for data transfer and remote control. The robot head position at a resolution of 0.1 µm and instantaneous velocity are stored on the PC at a default sampling rate of 92 Hz and can be used for later data processing.

2.1.2 Flat plate

The chosen blade geometry is a rectangular flat plate. The dimensions of the flat plate are 200 mm in length, 100 mm in width and 4 mm in thickness, as seen in Fig. 15(a). The plate is made of Plexiglas allowing for optical access and reducing reflections during PIV measurements. The translatory motion of the plate is along the x-axis from point P1 to P2, as seen in Fig. 14. The depth h is defined as the distance between the top of the flat plate to the air-water interface at rest, see Fig. 15(a). Three different depths h are considered throughout this work. These depths are listed in Table 1.

h (mm)	Scenario
0	Top of the flat plate coincides with the air/water interface
20	Flat plate is close to the air/water interface
100	Deep water case

Table 1. The three plate depths considered in the current work.

The position of the plate along the y-axis is kept constant, such that it coincides with the half width of the tank. The plate is connected to the robot head using a plate holder as shown in Fig. 15(b). The plate holder has a symmetrical streamlined cross section. This reduces the hydrodynamic disturbances due to the holder. The plate is held in a vertical plane (yz plane) such that the longest edges are parallel to the air/water interface, as seen in Fig. 15(b).

2.2 SENSORS AND DATA ACQUISITION

To measure the force acting on the flat plate during the runs from P1 to P2, two sets of data are acquired from the robot: path data and force data. Path data is available directly from the software module ProVis installed on the PC connected to ROBOTstarV. The raw Path data file includes the position and velocity of the robot head as a function of time. By default, the position and the velocity data are sampled at 92 Hz. Force/torque data are obtained from an ATI multi-axis force/torque transducer mounted between the robot head and the plate holder, as shown in Fig. 15(b). The transducer is operated through LabVIEW, and the force signal is sampled at a rate of 10 kHz. From Fig. 14 and Fig. 15(b), it can be seen that the movement of the plate along the x-axis will result in a force F_x acting in the x-direction, i.e., normal to the flat plate. The force F_x results in a torque about y-axis, T_y. Force measurements from the transducer have a lower signal-to-noise ratio than the torque measurements. Therefore, the torque about the y-axis is used for calculating the force in the x-direction on the plate.

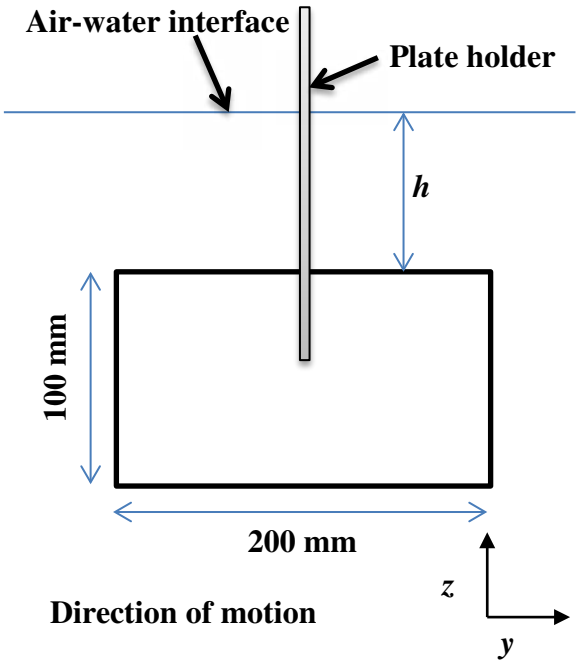

Fig. 15(a). Schematic of the flat plate shown in the *yz* plane.

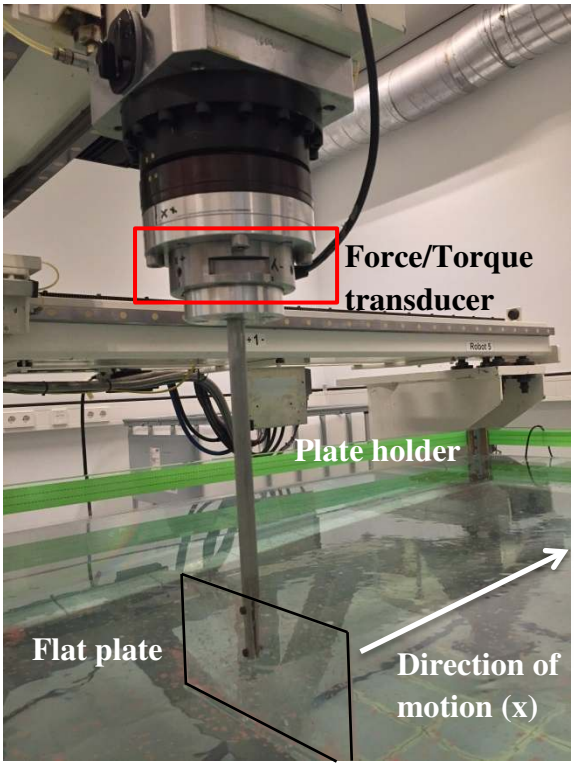

Fig. 15(b). The flat plate connected to the robot head.

The drag force F_D is thus determined as:

$$F_D = \frac{T_y}{L_c},$$

where we assume that the point of application of the force with respect to the robot head L_c is constant (L_c = 0.29 m). This was validated by calculating L_c from F_x and T_y for various runs.

Figure 16 shows a typical result from a test run for a plate depth of h = 100 mm. The drag force F_D and plate velocity V are plotted against time for a test run where the plate moves from position P1 to P2 (see Fig. 14). During the accelerating and decelerating phases, the plate has a constant acceleration of 100% and a default deceleration of 200% respectively. In between the acceleration and deceleration phases, the plate moves with a constant velocity of V = 300 mm/s.

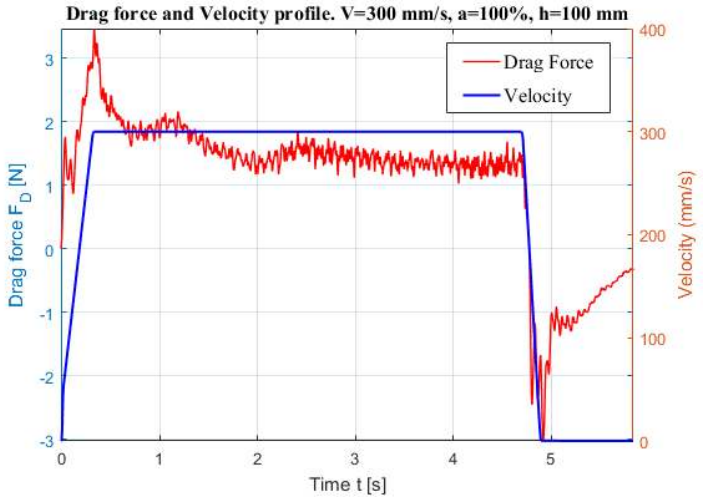

Fig. 16. Drag force and plate velocity vs time plot during a test run using data from the robot and the force/torque transducer.

2.3 HYDROGEN BUBBLE VISUALIZATION SETUP

To visualize the flow features around the flat plate, hydrogen bubble visualization is used. This technique is based on the electrolysis of water. During the electrolysis of water, hydrogen gas bubbles are formed at the cathode, which act as flow tracers. When properly illuminated, the images can be recorded with a camera, and used to study the flow.

In the present experiment, this method is implemented by placing the cathode on the front surface of the flat plate. A single copper wire with a diameter of 0.16 mm is used as the cathode. Two holes are drilled in the flat plate at each of the corners of five concentric rectangles. The copper wire is passed through these holes and held in tension, such that the wire arrangement is as shown in Fig. 17. By passing a direct current through two electrodes placed in the water, oxygen is produced at the anode, and hydrogen at the cathode. The anode used is a perforated stainless steel plate of length 1.8 m and 0.3 m width that is placed perpendicular to the flat plate, and at a distance of 0.3 m from the center of the flat plate, see Fig. 18.

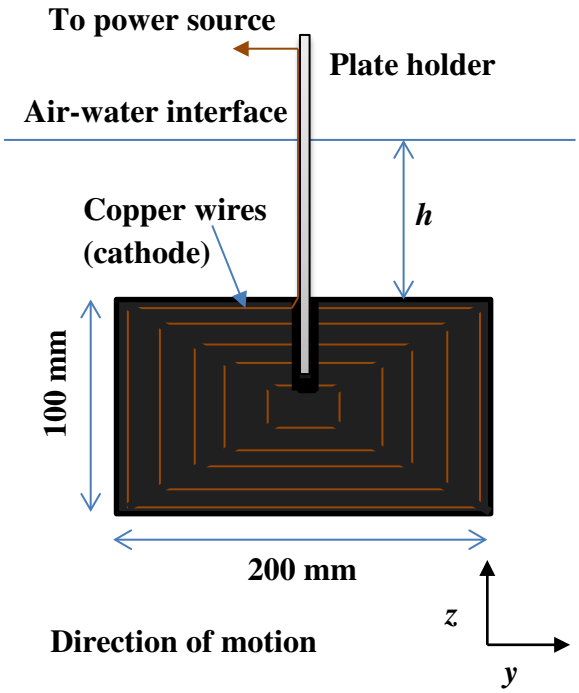

Fig. 17. Schematic of the flat plate with the cathode wire arrangement.

A constant voltage power source capable of producing a potential difference of 30 V and a current of 5 A is used. At a potential difference of 30 V an electrical current of 0.54 A passes through the electrodes when the tank is filled with normal tap water. At a current of 0.54 A the number of bubbles produced at the electrodes is too low for proper flow visualization. The number of bubbles produced is proportional to the electrical current passing through the electrodes, and this current can be increased by increasing the electrical conductivity of the fluid in the tank. An amount of 2.5 kg of Sodium Sulfate is then added to the 1.92 m^3 of water in the tank resulting in an increase of the electrical current to 2.2 A (at potential difference of 30 V). At this value of the electrical current, the number of hydrogen bubbles produced at the electrodes is sufficiently high for proper visualization of the flow.

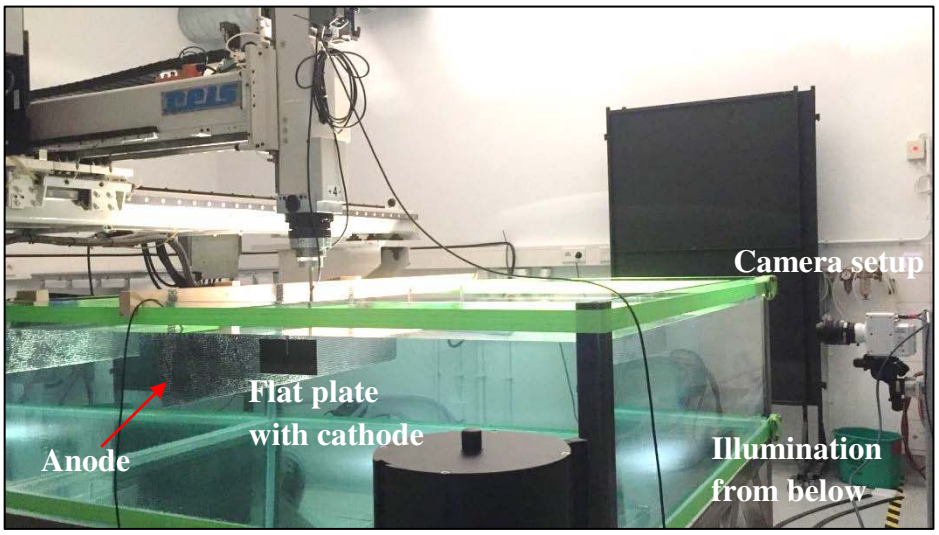

Fig. 18. Hydrogen bubble visualization setup.

The diameter of the hydrogen bubbles produced is of the order of one half of the wire diameter (Sabatino et al. [2012]). When a thinner wire is used, the current passing through the electrodes decreases. This can be compensated by either increasing the potential difference between the electrodes or by bringing the anode closer to the cathode. However, increasing the potential difference any further (above 30 V) could be a physical hazard. If the anode is moved closer to the cathode, it would affect the flow. This resulted in the current setup. The bubble size was sufficiently high for proper visualization of the flow. Also, it was found that the inclusion of hydrogen bubbles did not have a significant effect on the flow or the force/torque measurements, which is discussed in Appendix A.

To record the hydrogen bubble visualization, a 4 Megapixel Phantom VEO 640 high speed camera equipped with a 105 mm Nikon lens is used. The CMOS chip of the camera has a pixel size of 10 μm and a pixel format of 2560 × 1600. All images are captured at a frame rate of 500 fps unless otherwise stated. As shown in Fig. 18, the camera is placed on a rail, in front of the glass tank. This allows movement of the camera parallel to the plate path. The path of the flat plate is illuminated from below the tank using four 400 W wide beam floodlights. A typical image from the hydrogen bubble visualization is shown in Fig. 19. To improve the readability of the images, the b/w intensity values were inverted and the contrast of the camera images was adjusted which results in the image shown in Fig. 20. Also, the flat plate was painted black beforehand. Otherwise, the inversion of the b/w intensity values would result in a black plate in Fig. 20, decreasing the contrast between the bubbles and the plate.

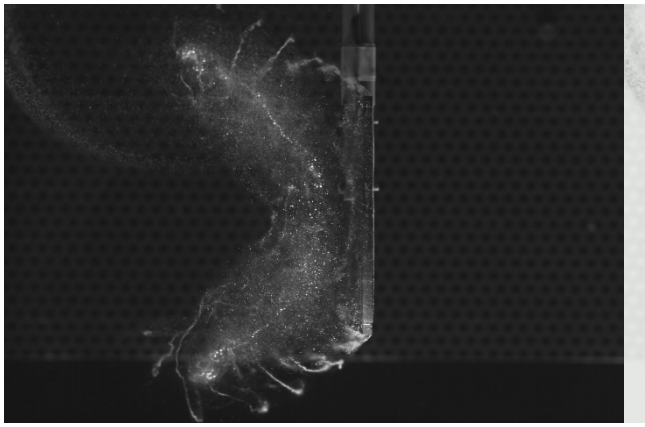

Fig. 19. Frame data from the hydrogen bubble visualization technique.

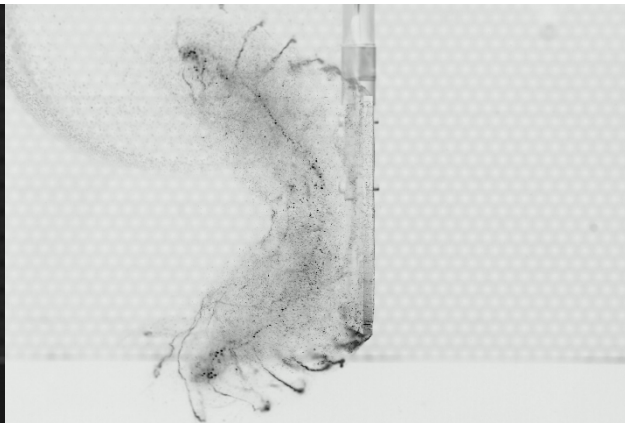

Fig. 20. Processed image after the inversion of b/w intensity values.

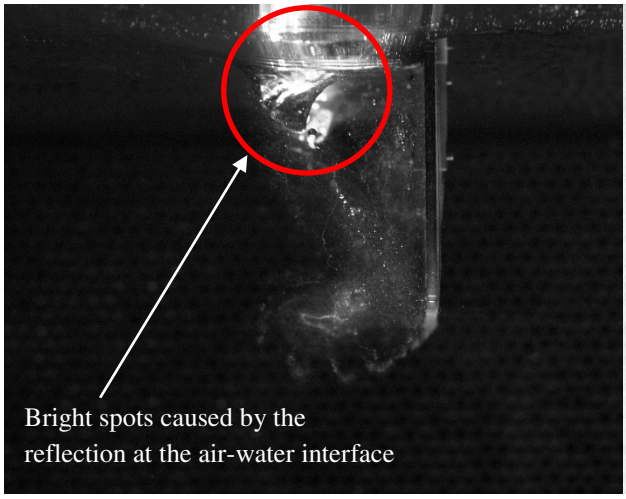

Fig. 21. Visualization when the flat plate is near the air-water interface.

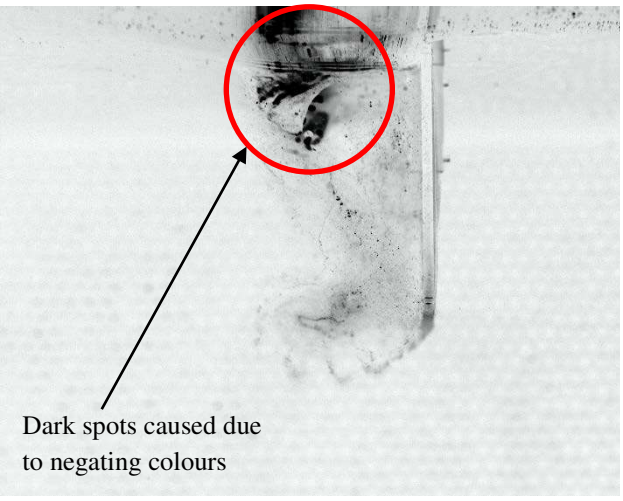

Fig. 22. Processed image with dark spots because of the disturbed air-water interface.

One major disadvantage of the hydrogen bubble visualization technique occurs when the visualization region includes a free surface. In the current work, the region of interest is illuminated from below. When visualizing the flow near the air-water interface, the strong vortices pull the air-water interface downwards. The disturbed air-water interface reflects the illumination causing very bright spots in the image, as illustrated in Fig. 21. When this camera image is inverted, it results in dark spots, in Fig. 22. This reduces the visibility of the bubbles, making it difficult to interpret. Nonetheless, the processed image still a better readability than the original image and is deemed sufficient for analysis.

2.3.1 Test matrix for hydrogen bubble visualization

The flow is visualized by using the hydrogen bubble visualization technique for the following configurations.

Plate velocity V (mm/s)	Depth below surface h (mm)	Acceleration (%)
200 (Re ≈ 4.0×10^4)	0	50
300 (Re ≈ 6.0×10^4)	20	100
400 (Re ≈ 8.0×10^4)	100	200

Table 2. Test matrix for hydrogen bubble visualization.

When compared to actual rowing, the Reynolds numbers in these configurations are almost ten times smaller. It is practically impossible to reach higher Reynolds numbers in the current setup. The available size of the test tank restricts any further increase in the size of the plate or in velocity. Also, increasing the velocity of the flat plate would result in sloshing and water spillage. However, the Reynolds numbers are sufficiently high and are thought to be well in the turbulent regime. Therefore, this setup suffices for the current work.

2.4 PIV SETUP

To obtain quantitative data of the flow features besides the qualitative data from the hydrogen bubble visualization, Particle Image Velocimetry (PIV) is used to determine the velocity fields around the plate. Figure 23 depicts the setup used during the PIV measurements. In the current work, a Nd:YLF Litron laser with a maximum output of 150 W at wavelength λ = 532

nm with a 100 ns pulse duration is used. The output beam from the laser is converted into a horizontal light sheet using a series of two cylindrical lenses of focal length -25 mm and -50 mm. The resulting light sheet has a thickness of approximately 1 mm, and covered the entire path of the flat plate. The laser and the high speed camera are synchronized using DaVis v8.4. Davis is also used to acquire and process the images recorded by the high speed camera. In the current work, fluorescent particles are used as tracers. 10 g of Fluorescent Red Polyethylene microspheres from Cospheric were added to the water. The size of these particles ranged between 53-63 µm with a density of 994.5 kg/m^3, allowing for neutral buoyancy.

A high speed camera is placed horizontally, below the bottom of the tank aimed at the field of view via a 45° inclined mirror. A 4 Mepapixel LaVision Imager Pro HS camera with a pixel size of 11 µm and a pixel format of 2016 × 2016 is used. The images are captured using a Nikon 35 mm lens with a f-stop of 5.6. For calibration purposes, a rectangular calibration plate of size 700 mm x 700 mm is mounted on the robot head. The calibration plate is positioned such that the calibration plane coincides with the horizontal mid-plane of the flat plate. The field of view achieved for this setup is 550 mm x 550 mm. This covers more than one-third of the motion of the flat plate (total span = 1400 mm, from P1 to P2). To record the entire motion, the camera-mirror setup is shifted from C1 to C2 and C3, see Fig. 23, and the experiment is repeated. This covers the entire plate path, with slightly overlapping field of view.

The images were acquired at a frame rate of 1 kHz. The velocity field was obtained by the cross-correlation of every nth and n+3th image. The processing is done using a 32 × 32 pixel interrogation window with a 50% overlap, which gives 170 × 170 vectors for each field of view with a spatial resolution of 3.2 mm × 3.2 mm. The motion of the flat plate is recorded as three different segments: C1, C2 and C3. The three segments are stitched together, using MATLAB, to study the entire motion of the flat plate. This stitching procedure is discussed in detail in Appendix B.

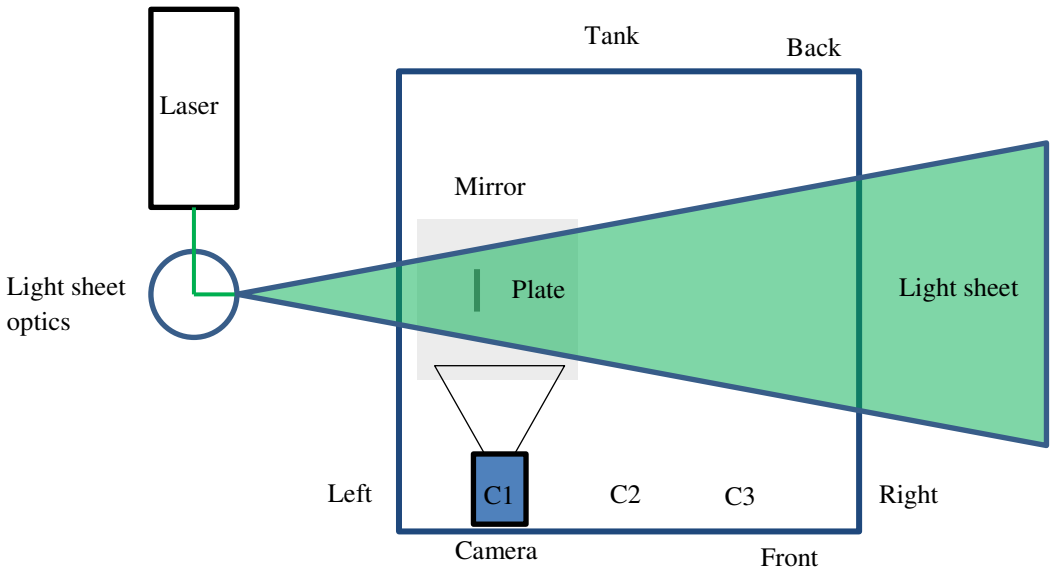

Fig. 23. Schematic top view of the PIV setup.

3

RESULTS AND DISCUSSION

This chapter presents and discusses the results from the hydrogen bubble visualization and particle image velocimetry experiments. For better understanding of the results, the terminology used is first explained. As defined earlier, *h* is the depth of the plate, which is the distance between the top face of the flat plate and the air-water interface at rest. The motion of the flat plate along its programmed path, from P1 at (x1, y1, *h*) to P2 at (x2, y1, *h*) in Fig. 14, is defined as the *run*. The *configuration* of a run is specified by the cruise velocity, acceleration and depth of the flat plate. Acceleration is defined as a percentage of the default robot acceleration, which is 0.82 m/s^2 (corresponding to 100% acceleration). The maximum achievable robot acceleration is 1.64 m/s^2 or 200%.

3.1 TORQUE/FORCE ON THE FLAT PLATE

The first run was performed for a configuration with h = 100 mm, V = 300 mm/s and 100% acceleration. For this run the Reynolds number (Re) based on the length of the flat plate is approximately 6.0×10^4. During the run, torque data is collected from the force/torque transducer and the path data is collected from the robot. The drag force on the plate was calculated from the torque data. The drag force data were then synchronized with the path data, starting in P1 at t = 0 and ending in P2 at t = 4.896 s.

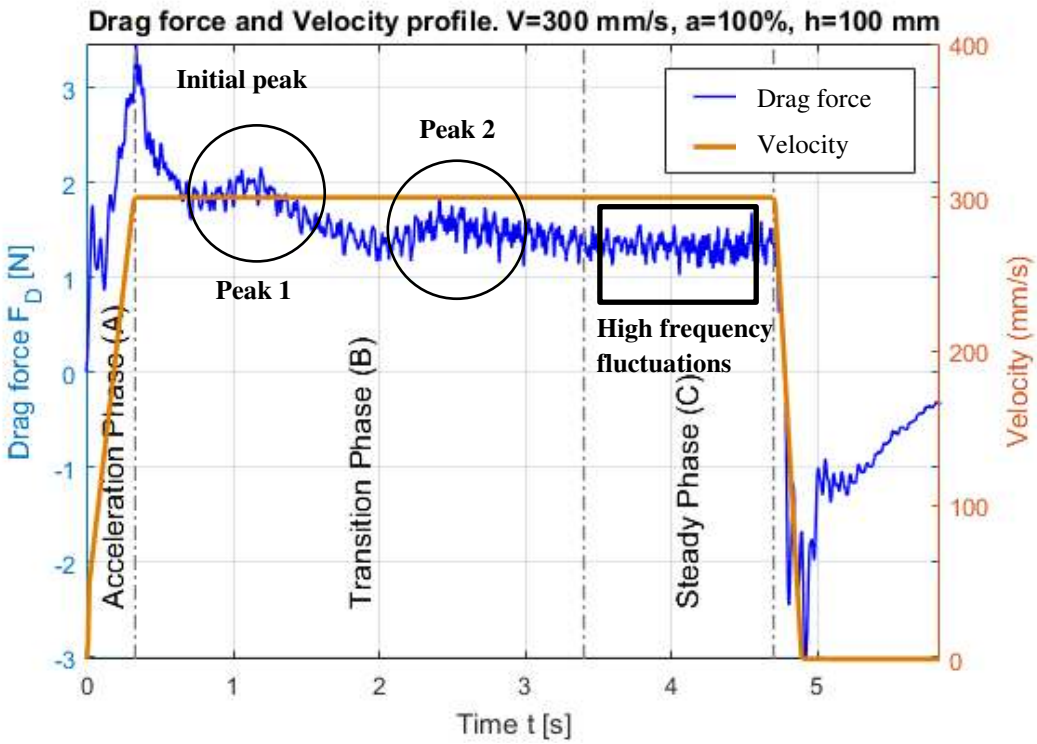

Fig. 24. Drag force and velocity data of an entire run.

Figure 24 depicts the drag force and the velocity of the plate as a function of time. From these profiles, it is observed that:

- At the start of the run, the plate accelerates from 0 to 300 mm/s. This phase is termed the *acceleration phase (A).* During this phase, the drag force on the plate rapidly increases. The drag force reaches a maximum at t = 0.331 s, which is very close to the time instant (t = 0.327 s) when the plate reaches maximum velocity. The maximum drag force on the plate near the end of the acceleration phase is called the *initial peak*.
- The acceleration of the plate through water results in an increased drag force because of the additional amount of water that has to be accelerated in addition to the mass of the plate. This added mass effect no longer exists when the plate stops accelerating, resulting in a steep decrease in the drag force after t = 0.331 s.
- The time period from t = 3.4 s and the instant when the plate starts to decelerate (at t = 4.7 s), is termed the *steady phase (C).* During this phase, the average drag force on the plate remains steady.
- The time period between the initial peak at t = 0.331 s and the start of the steady phase at t = 3.4 s is called the *transition phase (B)* and it includes two local maxima, denoted as *peak 1* and *peak 2*.
- When the plate starts to decelerate, the drag force on the plate decreases. The drag force becomes negative because the wake of the plate overtakes the decelerating plate. Maximum negative drag force is observed immediately after the plate comes to a complete stop.
- During the entire run, the drag force on the plate shows high frequency fluctuations. These fluctuations in drag force are visible, even after the plate has stopped. The origin of these high frequency fluctuations is discussed later in Sec. 3.6.

3.2 BASIC DECOMPOSITION OF THE FORCE ON THE PLATE

Based on the velocity profile and the drag force profile in Fig. 24, the force acting on the plate is decomposed into a drag force F_{CD} obtained from the steady phase C_D and a force due to a virtual mass (F_{VM}). The virtual mass is the sum of the mass of the plate m_p (m_p = 0.4 kg) and the added mass, m_a. These forces are calculated using the following relations:

$$F_{CD} = \frac{1}{2}\rho l_a l_b V^2 C_{D,steady\ phase}$$

$$F_{VM} = \left[m_a + m_p\right]\frac{dV(t)}{dt}$$

where V is the instantaneous velocity obtained from the velocity profile, l_a and l_b are the length and the width of the plate, respectively. The added mass m_a is determined from the expression proposed by Patton [1965]:

$$m_a = \frac{\rho k \pi}{4} l_a^2 l_b,$$

where k is the hydrodynamic mass factor (k = 0.826 for a 2:1 rectangular plate, Patton [1965]). The contribution of the forces F_{CD} and F_{VM} to the total drag force F_D is presented in Fig. 25.

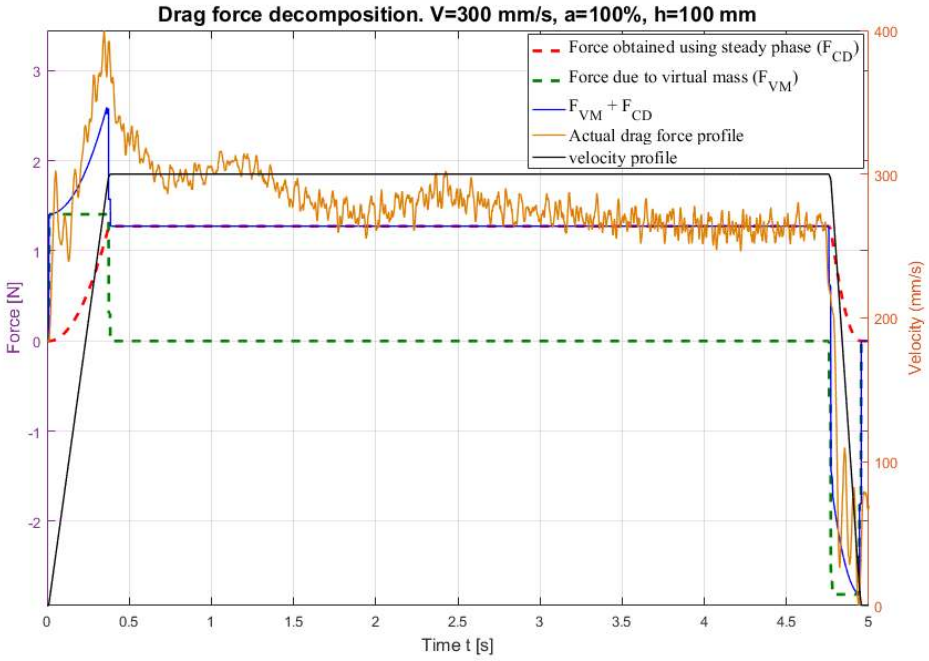

Fig. 25. Decomposition of the force on the flat plate.

It is observed that the force F_{VM} is present only during the acceleration phase of the plate and the force F_{CD} is present during the entire run and is proportional to the square of the velocity. The sum of these two forces result in a drag force profile that is qualitatively similar to the actual drag force profile in Fig. 25. This shows that the initial peak is a result of the added mass effect. However, there is a difference in the magnitude of the measured drag force and the decomposed drag force profile. The peaks 1 and 2 are not observed in the decomposed drag force profile. The cause for these discrepancies are unclear at this stage. A similar profile for F_{VM} was also observed with the relation for added mass proposed by Yu [1945].

3.3 EFFECT OF THE PLATE DEPTH ON THE DRAG FORCE

The analysis was extended to different values of the plate depth h, to identify differences in the drag force when the plate was closer to the air-water interface. Runs were carried out at three different depths (h = 0, 20 mm and 100 mm) for the same velocity (V = 300 mm/s) and the same acceleration (100%). The drag force profiles for these three cases are shown in Fig. 26. From the figure, it is observed that:

- During the acceleration phase (A), the drag force on the plate increases and reaches a maximum at the end of this phase for all three cases. Fluctuations in drag force during this phase are also very similar, but the magnitude varies as can be seen in the inset in Fig. 26.
- When the top of the plate is near the air-water interface (h = 0 mm), the drag force on the plate is significantly lower during most of the transition phase and during the steady phase. For the h = 0 mm case, the drag force reaches a steady state value earlier than the other cases. For the h = 20 mm case, the average drag force value is considerably higher, after t = 1.5 s.
- Significant differences between the three cases occur when the blade reaches its cruise velocity (t > 0.327 s). Two secondary peaks are observed during the transition phase for the h = 100 mm case. These peaks do not exist in the h = 20 mm case, while very mild secondary maxima can be discerned for the h = 0 mm case.
- In all three cases, the drag force exhibits high frequency fluctuations during the entire run. As mentioned earlier, these fluctuations will be discussed later in Sec. 3.6.

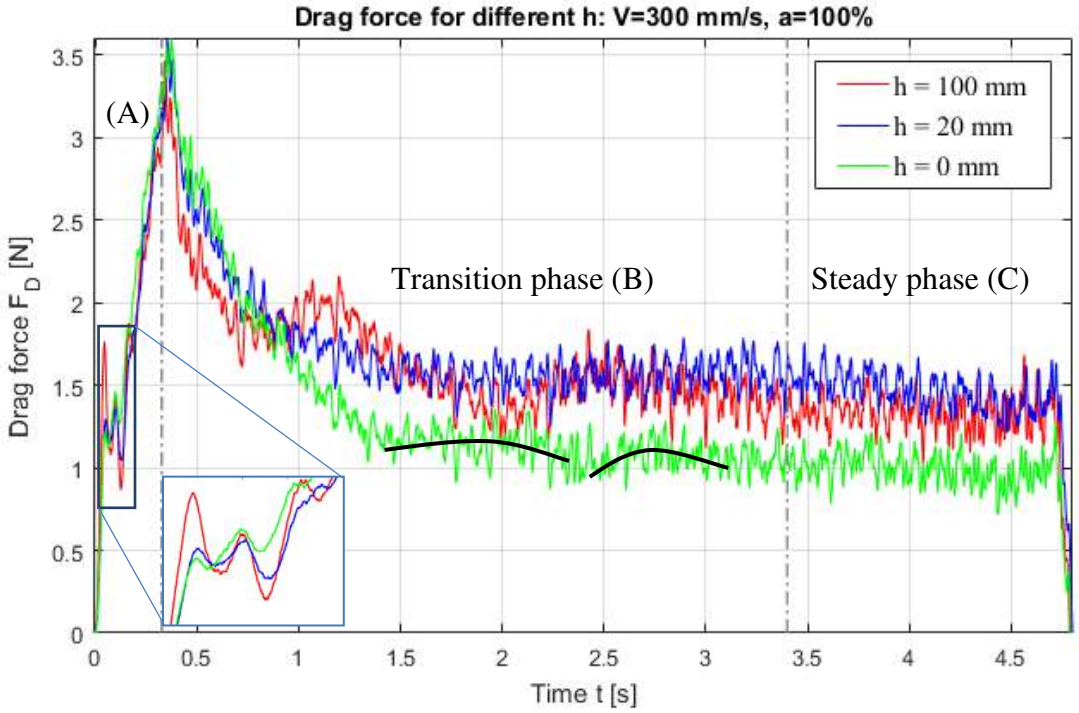

Fig. 26. Drag force profiles for different depths below the air-water interface, h.

From the drag force profiles in Fig. 26, the drag coefficient C_D (= $C_{D,\ steady\ phase}$) is calculated for each case by taking the average value of the drag force on the plate during the steady phase of the run. Figure 27 depicts the drag coefficient as a function of the plate depth h, between h = -50 mm and h = 200 mm for the configurations with V = 300 mm/s and 100% acceleration. To determine the reproducibility of the results, the measurements for each value of h were repeated. The mean difference in steady phase drag coefficient between two runs of identical configuration was 1.6% with a standard deviation of 1.4% indicating good reproducibility. Fig. 27 shows that maximum drag occurs at around h = 20 mm. As h increases beyond 20 mm, the drag coefficient gradually varies, and eventually stabilizes at a value of 1.3.

The configurations with depths h = 0 and h = 200 mm represent the two limiting cases. Clearly, for h = 0, the top face of the plate is at the air-water interface when the plate is at rest in stagnant water, while h = 100 mm is considered to be the "deep water" case. Previous experimental works with similar test conditions (such as Reynolds number and geometry) showed a drag coefficient value of 1.07 for the h = 0 mm case (Jacobs [1985]) and around 1.2 for the h = 100 mm case (Bearman [1971] and Ortiz et al. [2015]). From Fig. 27, it is observed that the drag coefficient value obtained in the present work compares well to the above references for the limiting cases, thereby validating the current setup. Therefore, three different depths of h = 0, 20 mm and 100 mm have been considered in the present work to analyse the influence of the air-water interface on the drag force.

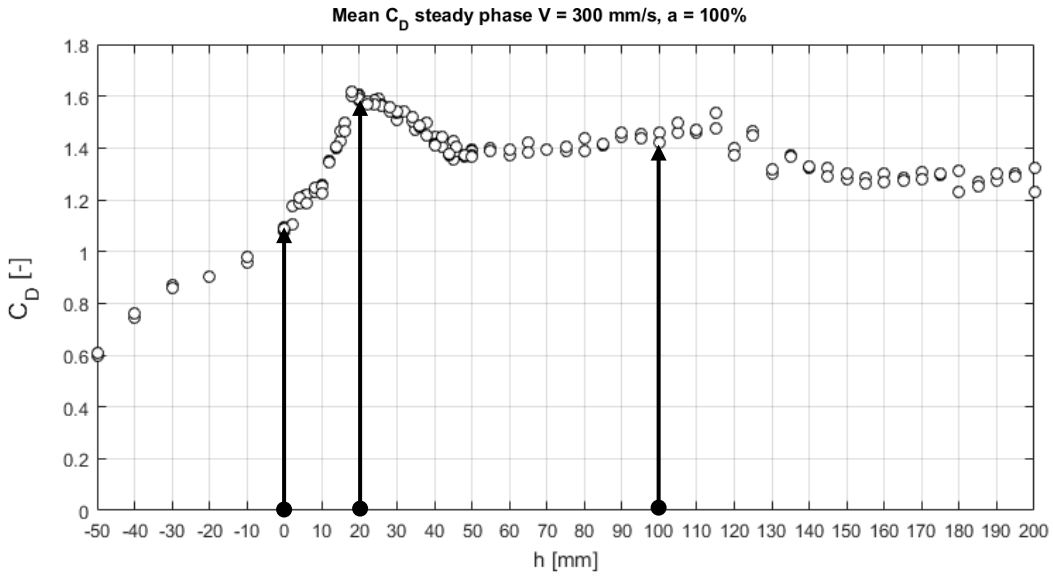

Fig. 27. Drag coefficient C_D for different depths *h* for a plate velocity of 300 mm/s and 100% acceleration.

3.4 EFFECT OF THE AIR-WATER INTERFACE

To determine the influence of the air-water interface on the plate, it is necessary to visualize the flow around the plate for different plate depths. This section presents and analyses the results of the hydrogen bubble visualization for the configurations with different depths (*h* = 0, 20 mm and 100 mm). The cruise velocity of the flat plate was set at 300 mm/s, corresponding to a Reynolds number Re ≈ 6.0×10^4, and the plate acceleration was set at 100%. Hydrogen bubbles were introduced at the front surface of the plate using the cathode wire arrangement described in Sec. 2.3. A high speed camera was used to record the flow around the flat plate during the hydrogen bubble visualization. During the visualization, the drag force data and path data were obtained from the transducer and robot, respectively. In addition, the effect of inclusion of hydrogen bubbles to the flow and the presence of a cathode on the flat plate on drag force measurement was found to be insignificant (refer Appendix A).

3.4.1 Overview of the base case (h = 100 mm)

Figure 28 shows the drag force on the plate as a function of time for the deep water case (*h* = 100 mm). This configuration is the farthest from the air-water interface and presumably best resembles a flat plate in a rectangular flow and therefore is considered the base case. The drag force signal is split into three phases (acceleration, transition and steady phase) as discussed in Sec. 3.1. Similar to the drag force profile, the flow visualization is also split into these three phases that are each characterized by a certain flow pattern.

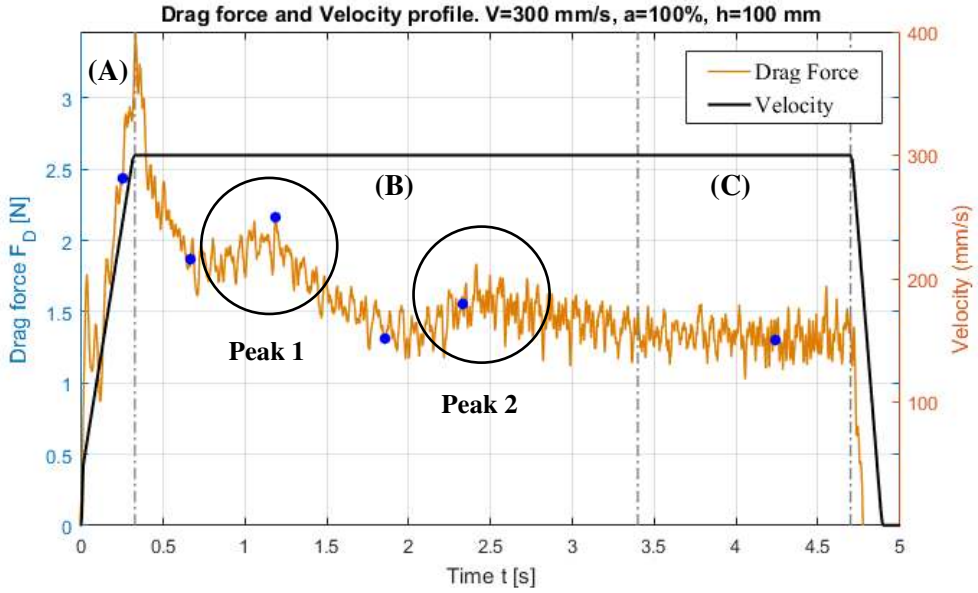

Fig. 28. Drag force and velocity profile for h = 100 mm at velocity 300 mm/s and 100% acceleration. Blue dots indicate the six time instants when the snapshots in Fig. 29 are taken.

During the acceleration phase, high pressure is expected to occur on the front side of the plate and the fluid moves along the front side towards the edges where the shear layer separates. This leads to the formation of vortices followed by its shedding from the faces, resulting in a vortex ring formation, as shown in Fig. 29(a). The vortex ring depicted here is shaped like a hyperellipse. With further movement of the plate, the vortex ring grows in size, as shown in Fig. 29(b).

During the transition phase, the vortex ring is stretched further in the streamwise direction. The shed vortices merge with the vortex ring up to approximately t = 1.186 s. From then on, the shed vortices flow into the space between the vortex ring and the plate. This creates a secondary vortex structure, as shown in Fig. 29(c). The time instant at which this shift in the behavior of the shed vortices occurs corresponds to peak 1 in the drag force profile, as shown in Fig. 28. The vortex ring moves away from the flat plate resulting in a decrease in its influence on the plate. This suggests the movement of a low pressure zone away from the plate, causing a decrease in the drag force. As time progresses, the vortex ring disintegrates, as shown in Fig. 29(d). These remnants cause the secondary vortex structure to circulate close to the plate, as shown in Fig. 29(d), (e). This secondary vortex structure results in a low pressure zone close behind the flat plate resulting in an increase in the drag force which corresponds to peak 2 in the drag force profile, as shown in Fig. 28.

During the steady phase, the interaction of the remnants of the vortex ring with the shed vortices is unnoticeable. The vortices no longer circulate close to the plate, as shown in Fig. 28(f). With the absence of strong low pressure zones close behind the plate, the drag force on the plate reduces and becomes steady, as shown in Fig. 28.

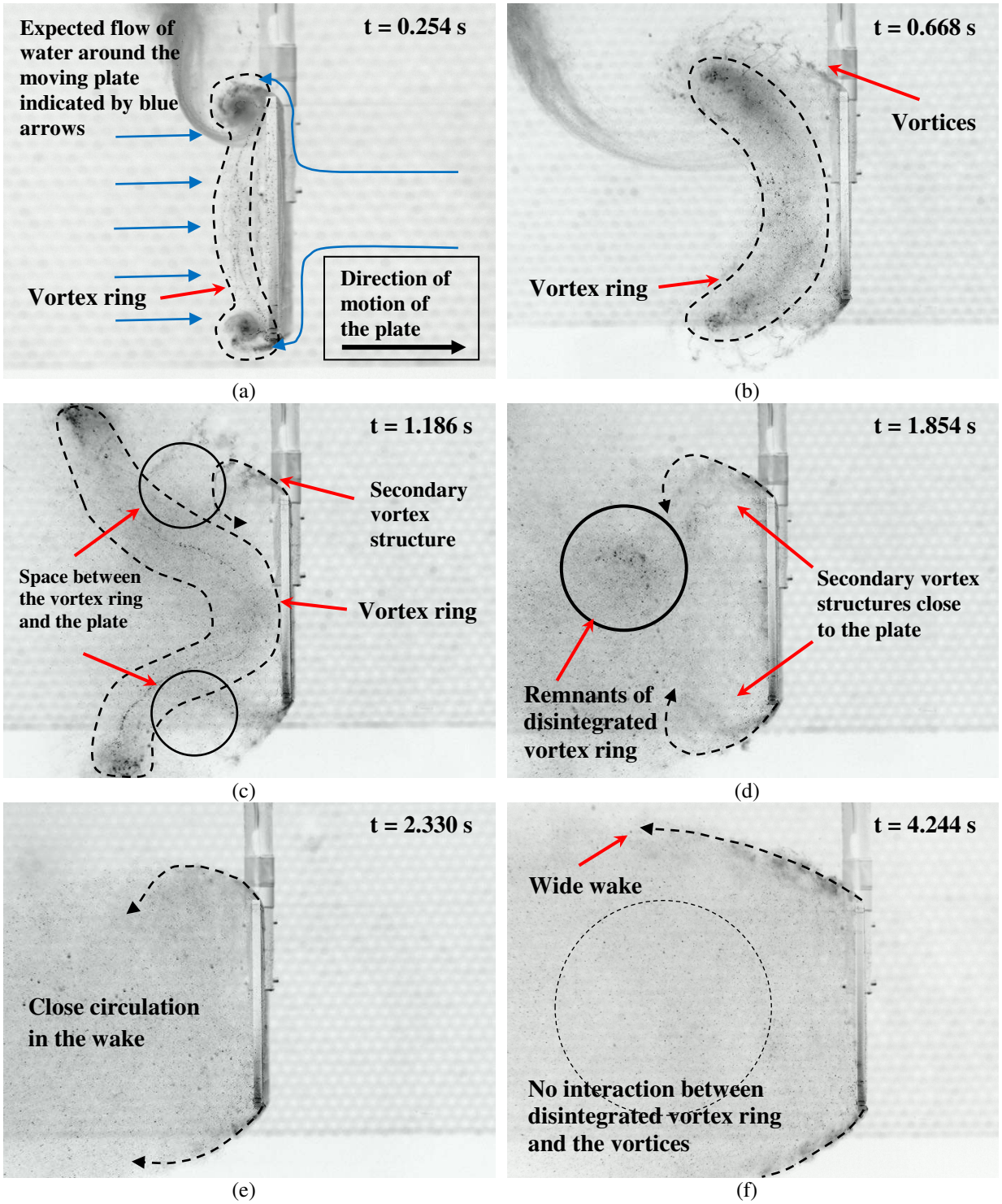

Fig. 29. Six instants of hydrogen bubble visualization for h = 100 mm at velocity V = 300 mm/s and 100% acceleration.

3.4.2 Differences between the base case (h = 100 mm) and the configurations with h = 0 and h = 20 mm

The base case is compared to the h = 0 and h = 20 mm cases. Since the only difference between the three cases is the depth h, the comparison of the visualization results identifies the differences due to the presence of the air-water interface. The drag force profiles for h = 0 mm and h = 20 mm are shown in Fig. 30 and Fig. 31, respectively. The drag force profiles show that there are no distinct peaks (peaks 1 and 2) after the initial peak.

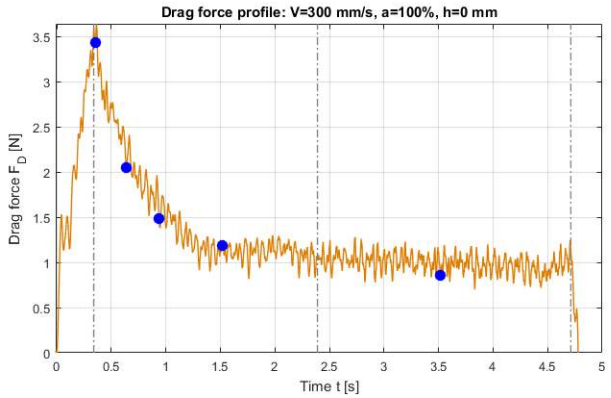

Fig. 30. Drag force profile for h = 0 mm at velocity 300 mm/s and 100% acceleration. Blue dots indicate the four time instants when the snapshots of the 0 mm case in Fig. 32, 33 and 34 are taken.

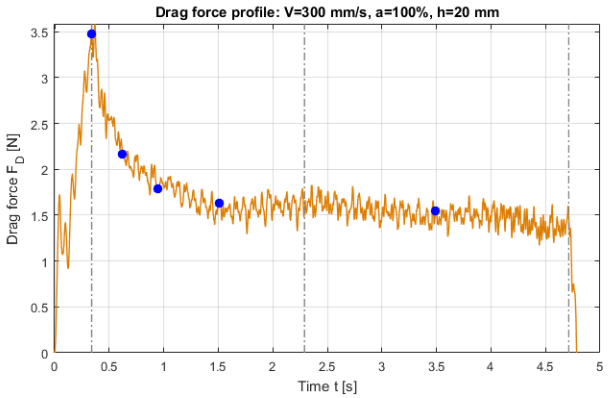

Fig. 31. Drag force profile for h = 20 mm at velocity 300 mm/s and 100% acceleration. Blue dots indicate the four time instants when the snapshots of the 20 mm case in Fig. 32, 33 and 34 are taken.

In the h = 0 mm case, the top face of the plate coincides with the air-water interface. Therefore, during the acceleration of the plate, the formation of a closed hyperelliptical vortex ring, like in the base case, is prevented. Instead, a U-shaped starting vortex with the free ends attached to the air-water interface is formed, as shown in Fig. 32(a). These ends produce strong depressions of the air-water interface behind the plate and the depression caused by one free end is shown in Fig. 32(a). During the acceleration, the initially vertical starting vortex becomes skewed, tilting away from the top face of the plate. The flow features near the bottom half of the plate are similar to those in the base case. In the h = 20 mm case, the plate is close to the air-water interface. The movement of the plate creates a vortex ring and also causes a trough-shaped depression of the air-water interface, as seen in Fig. 32(b), which extends in the spanwise direction. The flow over the top face of the plate results in the streamwise stretching of the top portion of the vortex ring. The flow features near the bottom half of the plate are again similar to the base case. Comparing these observations with the base case shown in Fig. 29(a), it is evident that the depth of the plate strongly affects the formation and the development of the vortex ring.

The major difference in the drag force profiles of the three cases occur during the transition phase, wherein there are no distinct peaks in the h = 0 mm and h = 20 mm cases. During the first half of the transition phase in the h = 0 mm case, the free ends of the U-shaped starting vortex shift away from the plate, as shown in Fig. 33(a). Also, a cloud of hydrogen bubbles is seen close to the back surface of the plate. From the consecutive camera images, this cloud was perceived as a small, circulating zone moving vertically downwards. The interaction of this cloud with the starting vortex resulted in the disintegration of the latter, as shown in Fig. 33(c). Also, the secondary vortex structure formed during the base case, shown in Fig. 29(c), cannot be identified in this case.

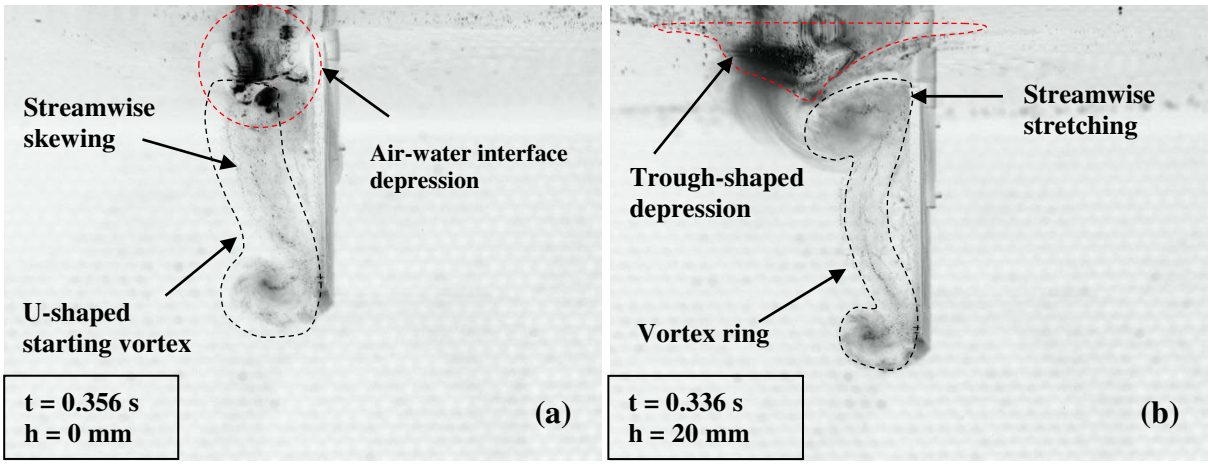

Fig. 32. Hydrogen bubble visualization near the end of phase A for (a) the 0 mm case and (b) the 20 mm case.

In the h = 20 mm case, the streamwise stretching of the top portion of the vortex ring continues during the start of the transition phase, as shown in Fig. 33(b). This resulted in the disintegration of the vortex ring, as shown in Fig. 33(d). During this process, the formation of the cloud of bubbles is not observed indicating no circulation zone, otherwise collecting the bubbles, is present. In Fig. 33(d), the concentration of hydrogen bubbles close to the back of the plate is merely a portion of the disintegrated vortex ring. The vortices, shed at the bottom of the plate, flow into the space between the plate and the disintegrated vortex ring, but this does not result in a secondary vortex structure. Instead of circulating close to the plate, as observed in the base case, the vortices shift away from the plate due to the influence of the remnants of the vortex ring, as shown in Fig. 33(d).

In both cases, h = 0 mm and h = 20 mm, the formation and development of the vortex ring is restricted due to the presence of the air-water interface. Also, a secondary vortex structure is not observed after vortex ring disintegration. Therefore, the peaks 1 and 2 in the drag force profile are not observed.

During the second half of the transition phase in the h = 0 mm case, the disintegrated starting vortex is relatively close to the plate compared to the base case, as shown in Fig. 33(e). The vortices shed at the bottom half of the plate roll over these disintegrated structures, resulting in a wide wake. For the h = 20 mm case, the disintegrated vortex ring shifts away reducing its influence on the vortices. However, the movement of the plate results in a V-shaped depression of the air-water interface which extends in the spanwise direction (marked as a solid line in Fig. 33(f)). The flow between the top face of the plate and the V-shaped depression is angled vertically downwards causing the vortices to circulate close to the plate. This suggests that the narrow gap above the plate in the h = 20 mm case plays an instrumental part in the circulation of shed vortices close to the plate.

During the steady phase, the drag force profiles show that the steady state value of the drag force is highest for the h = 20 mm case and lowest for the h = 0 mm case. Also, the steady phase is reached sooner for both these cases when compared to the base case. This is attributed to the vortex ring and the secondary vortex structure in the base case, which delays its steady phase.

For the h = 0 mm case, the wake contour in the bottom half of the plate is similar to that of the base case, as shown in Fig. 34(a). The top face of the plate creates continuous depressions of the air-water interface. Since the plate is at the air-water interface, the volume of water that needs to be displaced is lower when compared to the base case. This could explain the

decrease in the steady state drag force for the h = 0 mm case. For the h = 20 mm case, the wake profile in the bottom half of the plate is again similar to the base case. The vortices shed at the top of the plate continue to circulate close to the plate, as shown in Fig. 34(b). This results in a relatively strong low-pressure zone close to the plate. Therefore, it is concluded that the higher drag force observed in the steady phase of the h = 20 mm case is due to the compact wake.

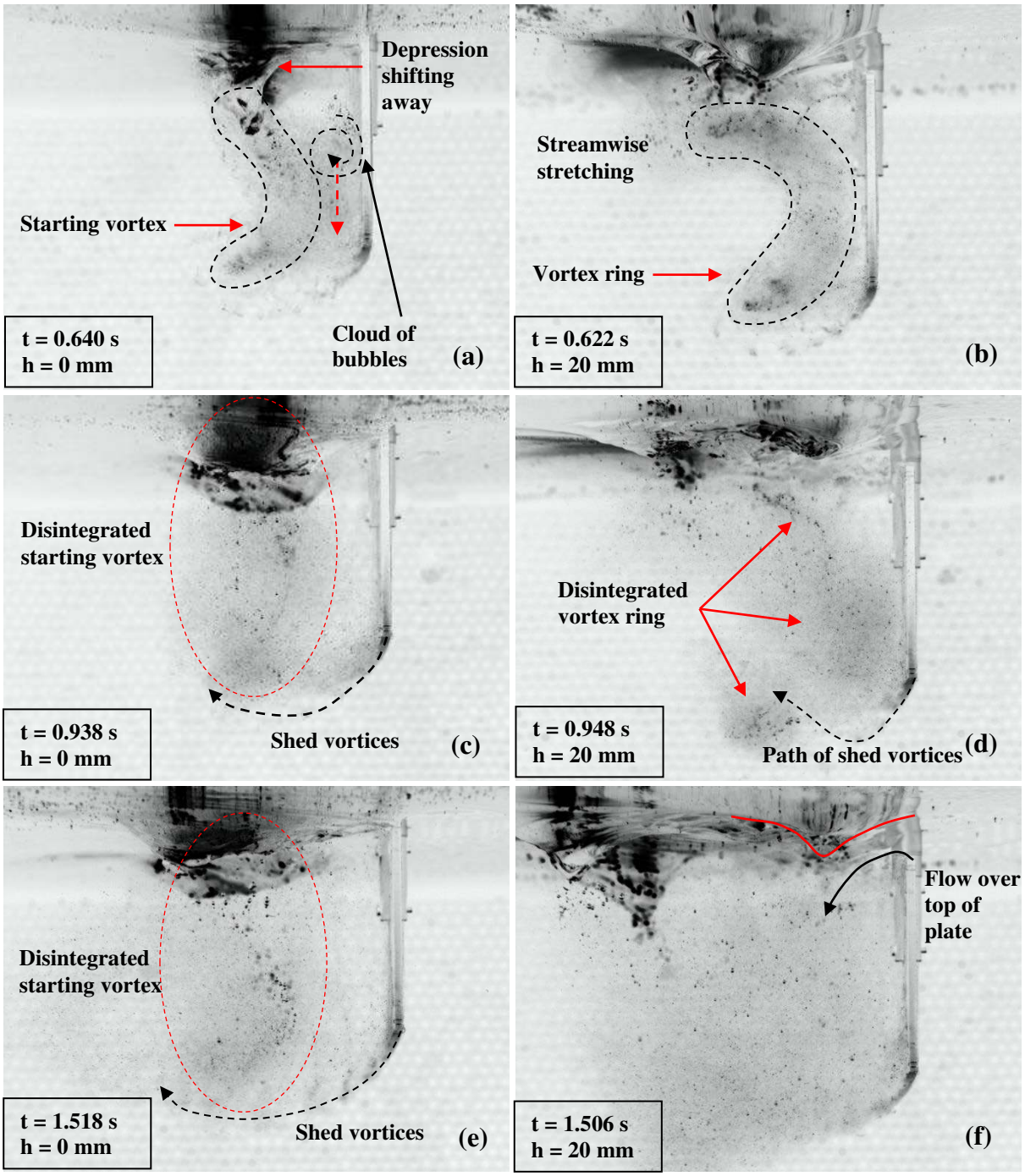

Fig. 33. Hydrogen bubble visualization during phase B for (a), (c), (e) 0 mm case and (b), (d), (f) 20 mm case.

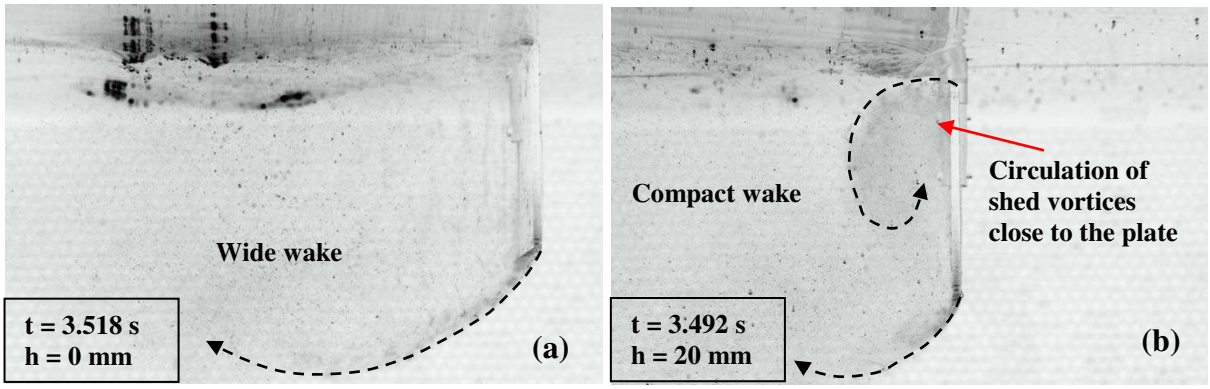

Fig. 34. Hydrogen bubble visualization during phase C for (a) 0 mm case, (b) 20 mm case.

3.5. EXTENSIVE DECOMPOSITION OF THE DRAG FORCE PROFILE

The analysis of the flow behaviour with respect to the drag force profile in Sec. 3.4 led to the correlation of flow characteristics to the drag force variations, such as peaks 1 and 2. The decomposition of the drag force signal suggested that there are significant differences in the actual drag force profile when compared to theory, as discussed in Sec. 3.2. It was observed that during the acceleration of the plate, the increase in the drag force was steeper than expected reaching a higher maximum when compared to the theoretical expectation. In addition, a slow decay of the drag force after the plate reached the cruise velocity was also observed. Since the origin of these additional forces is unclear, the focus was on the determination of the factors influencing these discrepancies. Therefore, the following experiments were done: drag force measurements for three depths considered (h = 0, 20 mm and 100 mm), for all possible combinations of five different velocities (V = 200, 250, 300, 350 and 400 mm/s) and seven different accelerations (50, 75, 100, 125, 150, 175 and 200%). It should be noted that these drag force signals were filtered (using a *sgolay filter*), since the high frequency fluctuations are not of interest at this point and the filtered signal improves the readability of the drag force signal. Figure 35 shows the drag force profiles for all 35 cases for the configuration with h = 0 mm up to t = 2 s. After this time, the drag force reaches the steady phase. The length of the steady phase is dependent on the velocity of the plate. It should be noted that in Fig. 35, the drag force signals for cases with the same acceleration are depicted with a single colour. Therefore, to better understand the difference in drag force signal caused by a change in velocity, Fig. 36 shows the drag force profile for the configuration with h = 0 for 100 % acceleration and all five velocities.

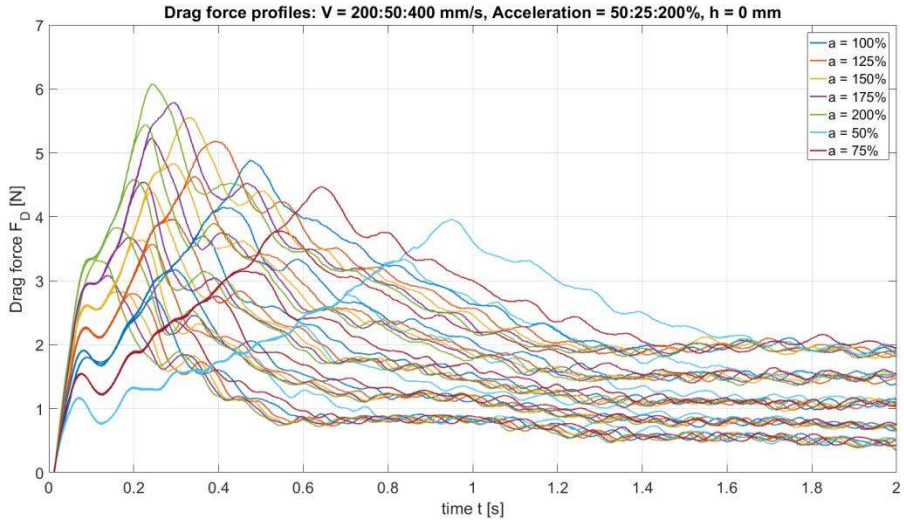

Fig. 35. Drag force profiles for the configuration with h = 0 mm for different velocities and accelerations.

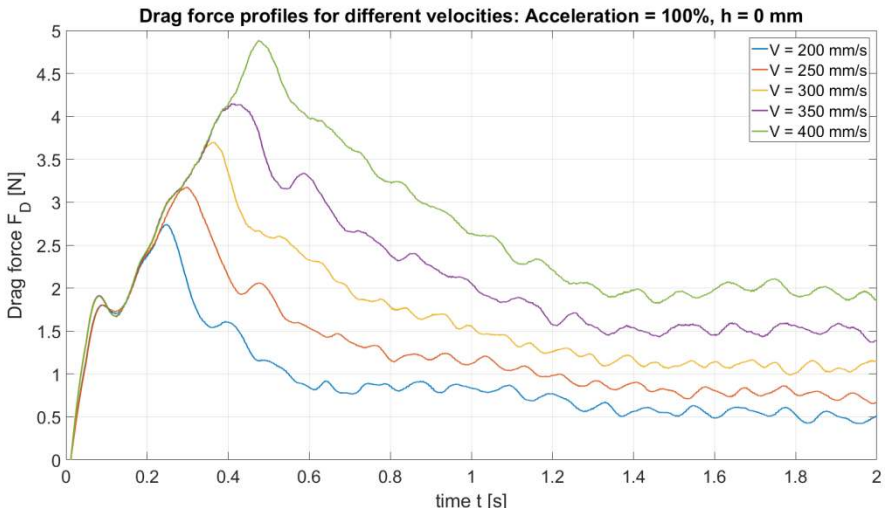

Fig. 36. Drag force profiles for the configuration with h = 0 mm and acceleration = 100% for different velocities.

Figure 36 shows that during the acceleration phase, the drag force signals follow the same curve until the cruise velocity is reached. Also, it is observed that with increase in the velocity, the maximum force attained is higher. After the plate reaches the cruise velocity, the drag force starts decaying eventually reaching the steady phase. The behaviour of the drag force observed for the other accelerations are also similar as can be seen in Fig. 35. An additional observation is that with an increase in the acceleration, the slope of the drag force profile in the acceleration phase increases, as can be seen in Fig. 35. As the plate reaches the steady phase, the drag force profile for each velocity collapses to nearly a single line irrespective of the plate acceleration. Thus, five lines for the five velocities is observed in Fig. 35 after approximately t = 1.8 s.

It can be seen from Fig. 35 that there is a correlation between the velocity, the acceleration and the drag force profile. Therefore, an attempt to model the behaviour of the drag force has been made, which gives a better decomposition of the forces acting on the plate.

3.5.1.Drag force decomposition

The drag force F_D acting on the plate is split into a steady and an unsteady component. As mentioned earlier, the drag force profiles collapse to a single line for each velocity irrespective of the acceleration, when the plate reaches the steady phase. Thus, it is relatively easy to model this phase of the run. Using the steady phase C_D, the steady drag force is modelled as

$$F_{CD} = \frac{1}{2}\rho l_a l_b V^2 C_{D,steady\ phase}$$

where V is the velocity of the plate.

Therefore, for any given velocity profile and steady phase C_D, the contribution of the force F_{CD} to the total drag force F_D can be determined. The force F_{CD} has been subtracted from the drag force profiles resulting in Fig. 37.

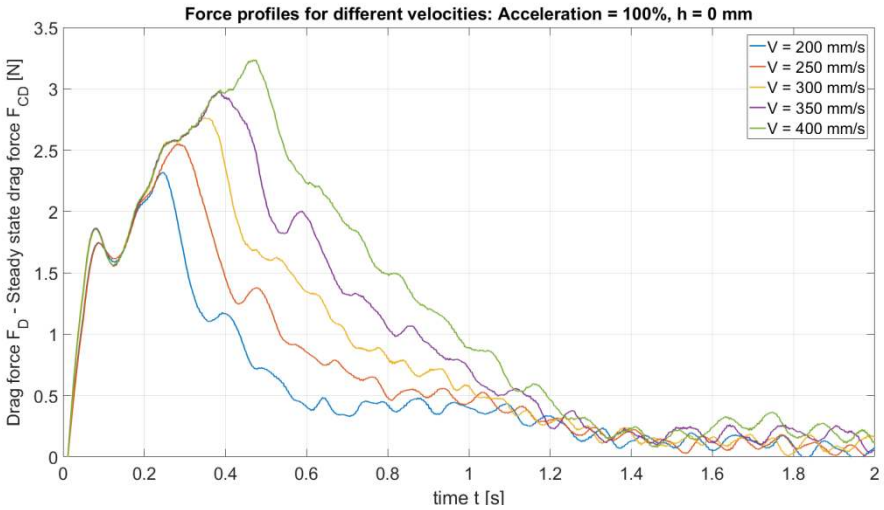

Fig. 37. Force profiles for the configuration with h = 0 mm and acceleration = 100% for different velocities.

In Sec. 3.2, the drag force signal was decomposed into two forces, namely the steady phase drag F_{CD} and the force due to the virtual mass F_{VM}. The force F_{CD} scales with the square of the velocity, while the force F_{VM} scales with the acceleration. For the current velocity profile, there is a period of constant acceleration followed by a period of constant velocity, see Fig. 28. Therefore, during the acceleration phase, the force F_{VM} is constant, and the force F_{CD} increases with increasing plate velocity. However, the subtraction of the force F_{CD} from the drag force profile resulting in Fig. 37 shows that the drag force is still increasing with time. Therefore, the removal of the constant force F_{VM} would still result in an increasing force during the acceleration phase. This shows the existence of a force, which increases in time, as long as the plate accelerates. This suggests that the force due to added mass is not constant, but rather time dependent in this case. Therefore, in the current decomposition, the force during the acceleration phase is decomposed as follows:

$$F_A = F_{MP} + F_{AM}$$

where, F_A is the force due to acceleration, F_{MP} is the force due to the acceleration of the mass of the plate and F_{AM} is the force due to acceleration of the added mass, which includes both the constant and time dependent added mass.

On the other hand, the force F_{VM} does not exist after the plate reaches constant velocity, and the force F_{CD} has already been removed in Fig. 37. Yet, after the peak, a gradual decay of the force is observed. This decaying force F_{DECAY} is also unaccounted for in the basic decomposition of the drag force profile in Sec. 3.2.

3.5.2. Modelling the acceleration phase

The drag force behaviour during the acceleration phase is modelled using the following forces:

- F_{CD}: This force is already defined in Sec. 3.5.1.

- F_{MP}: The force due to acceleration of the mass of the plate is defined as

  $$\mathrm{F_{MP}} = m_p a$$

  where m_p is the mass of the plate and a is the acceleration of the plate.

- F_{AM}: The force due to the added mass, including both the constant and the time dependent components. After removal of F_{MP} from the force profile in Fig. 37, the

remaining force profile fits a linear equation of the following form:

$$F_{AM} = At + B$$

where t is the time until the plate reaches the cruise velocity, and A and B are the coefficients obtained from the fit.

The unfiltered drag force signal for the configuration with depth h = 0 mm, V = 400 mm/s and 100% acceleration is used to determine the fit for the force F_{AM}. First, the contributions of the forces F_{CD} and F_{MP} are removed from the unfiltered drag force signal. Then, a linear fit with 95% confidence for the force F_{AM} is made, which yielded an adjusted R-square value of 0.7798. It was observed that the fit agreed well with the behaviour of the force F_{AM} with time.

It was seen earlier in Fig. 35 that during the acceleration phase, the drag force profile becomes steeper as acceleration increases. The same effect was observed with the force F_{AM}. Therefore, a different fit was required for every acceleration. This would thus result in seven different fits for the seven different accelerations, resulting in seven different values for the coefficients A and B. Figure 38 shows the force F_{AM} as a function of time for the configurations with V = 400 mm/s and the seven different accelerations. The adjusted R-square values of the fits for all the configurations range from 0.7289 to 0.8180. The relatively lower adjusted R-square values is due to the fluctuations in the drag force signal.

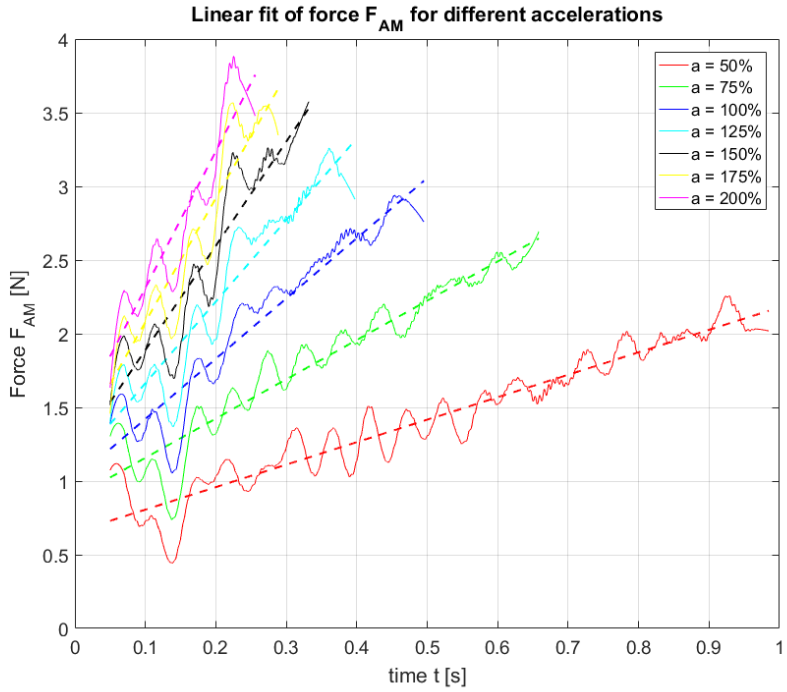

Fig. 38. Linear fits of the force F_{AM} for the configurations with V = 400 mm/s and h = 0. Solid lines represent the force profiles and the dotted lines represent the corresponding linear fits.

A close observation of the linear fits in Fig. 38 suggests that the slopes are correlated with acceleration a. Figure 39 presents the coefficients of the seven fits as a function of acceleration, which shows a linear relationship. Therefore, the coefficients were also modelled using a linear equation of the following form:

$$A = c_1 a + c_2$$
$$B = c_3 a + c_4$$

where a is the magnitude of the acceleration. The linear fits with 95% confidence for the coefficients A and B yielded adjusted R-square values of 0.9955 and 0.9439, respectively.

These high values are indicative of a strong linear relationship between the coefficients and the acceleration. A similar modelling procedure was followed for the h = 20 and 100 mm cases, and the resulting coefficients given in the table below.

Coefficients	h = 0 mm	h = 20 mm	h = 100 mm
c_1	6.578	7.419	5.952
c_2	-1.225	-1.388	-0.8996
c_3	0.5320	0.3180	0.8514
c_4	0.5226	0.5003	0.09225

Table 3. Linear fit of the coefficients A and B.

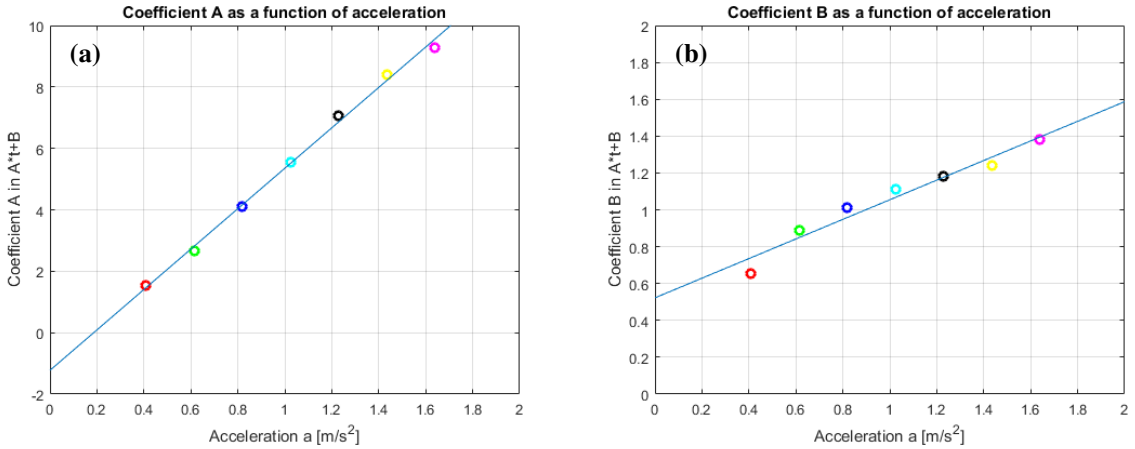

Fig. 39. (a) Linear fit of coefficient A, (b) Linear fit of coefficient B.

To summarize, the drag force during the accelerating phase is modelled as:

$$F_A = F_{CD} + m_p.a + (c_1 a + c_2)t + c_3 a + c_4$$

with the values of c_1, c_2, c_3 and c_4 given in Table 3.

The resulting model is compared to actual drag force profile in Fig. 40. The comparison shows that the model describes the actual drag profile during the acceleration phase quite well. Therefore, knowing the velocity, acceleration and the corresponding steady phase drag coefficient, it is possible to model the behaviour of the force acting on the plate during the acceleration phase and the steady phase.

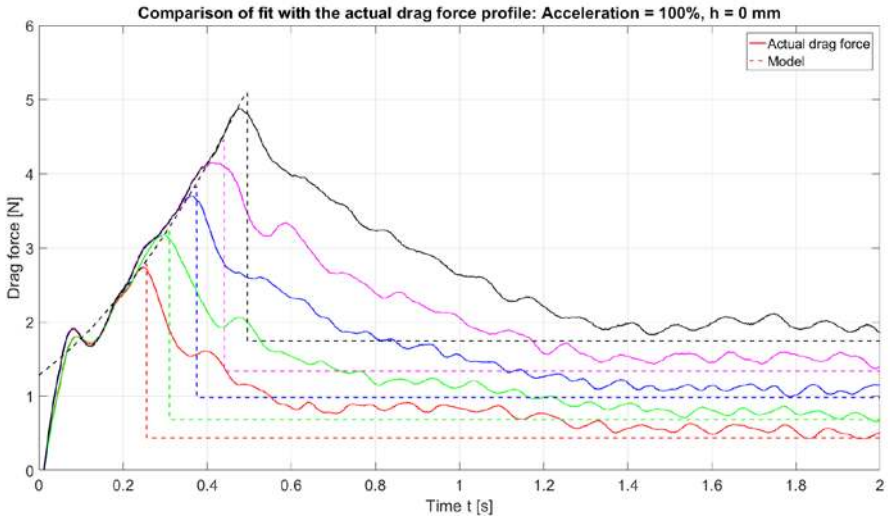

Fig. 40. Comparison of fit with the actual drag force profile.

Similarly, attempts were made to model the transition phase. As can be observed in Fig. 40, there is a gradual decay of the drag force. Even though the decay of the drag force follows a similar trend, the rate at which it decays is quite different for different velocities. This is also observed in Fig. 37, where the decay starts at different peaks but reach zero at approximately t = 2 s. It should be noted that the profiles in Fig. 37 correspond to a single acceleration, i.e. a = 100%. For different accelerations, the decay rates kept varying but the drag force profiles were also found to reach zero at approximately t = 2 s. This indicates that this decay rate strongly depends on the acceleration and the velocity, which affects the magnitude of the initial peak. However, in general, the behaviour of these decay curves was found to be like the function $1/t^n$, where n seems to vary from 0.5 to 2. An exact fit could not be determined.

Another approach to model the force F_{DECAY} is to use a non-dimensional time t_{nd} referred to as the formation number (Gharib et al. [1998]):

$$t_{nd} = \frac{V_{rm} \times t}{D}$$

$$V_{rm} = \frac{1}{t}\int_0^t V(t)dt$$

where t_{nd} is the non-dimensionalized time, V_{rm} is the running mean of the plate velocity, D is the thickness of the plate and V is the instantaneous velocity obtained from the velocity profile.

Figure 41 shows the drag force profile as a function of the non-dimensional time t_{nd}, for the configurations h = 0 mm, V = 300 mm/s and three different accelerations (50, 100 and 200%). It is observed that the acceleration phase of the drag force profiles no longer follows the same curve. However, the transition phases seem to collapse on a single curve. Upon further analysis, it was observed that this decay curve could not be modelled to the same level of accuracy as was done for the acceleration phase.

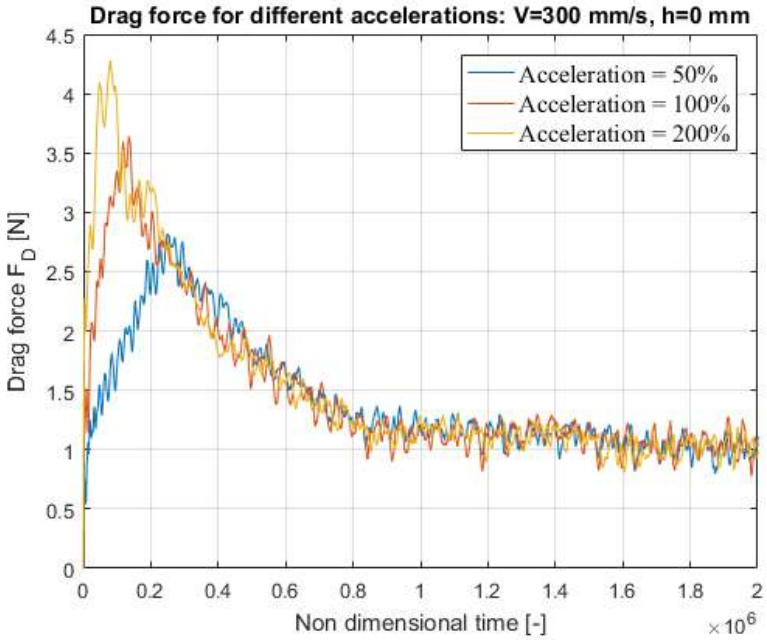

Fig. 41. Drag force as a function of non-dimensional time.

Therefore, the final model for the drag force excluding F_{DECAY} is as follows:

$$F_D(t) = \begin{cases} \frac{1}{2}\rho l_a l_b V(t)^2 C_{D,steady\ phase} + m_p a + (c_1 a + c_2)t + (c_3 a + c_4), & t < t_c \\ \frac{1}{2}\rho l_a l_b V(t)^2 C_{D,steady\ phase}, & t > t_c \end{cases}$$

where t_c is the time when the plate reaches the cruise velocity and F_{DECAY} is not included in the model but exists only after time t reaches t_c.

3.5.3. Physical significance of the forces F_{AM} and F_{DECAY}

In general, with a constant acceleration, the force due to the added mass component is considered constant. In the current scenario, it is observed that the force due to the acceleration is not constant. It can be seen from the force F_{AM}, that there is a constant (c_3a) and time dependent term (c_1at). The term c_3a resembles the conventional force due to the added mass. The term c_1at is considered the time dependent added mass force. The origin of such a force component could be explained by taking into account the vortex structures that travel along with the plate. When the plate accelerates, it was seen that a starting vortex is formed. This starting vortex seems to travel along with the plate, at least during the acceleration phase. At the same time, the size and the strength of this starting vortex seems to increase (see Sec. 3.7). Therefore, the plate along with the starting vortex could be envisioned as altering the effective geometry of the plate. This increasing size of the effective geometry is the reason for a different added mass component that also increases with time. Therefore, in the current scenario, this is experienced as an unsteady force due to the added mass. The origin of the offsets (c_2t and c_4) is difficult to postulate.

The origin of the force F_{DECAY} is due to the presence of the starting vortex. After the plate reaches the cruise velocity, the starting vortex shifts away from the plate, thus decreasing its influence on the drag force. The resulting influence on the flat plate is termed as the force F_{DECAY}. As mentioned earlier, this decay has a complex relation with the acceleration and the cruise velocity of the plate, which could not be determined. Therefore, it has not been modelled in the current analysis.

3.6 VORTEX SHEDDING FREQUENCIES

The results of the hydrogen bubble visualization technique and the decomposition of the drag force behaviour has provided a correlation between the large vortex structures and the drag force. However, throughout the run, high frequency fluctuations of the drag force are observed. These fluctuations appear to be correlated with the vortex shedding during the run. To determine the relation, dominant frequencies of the drag force fluctuations are determined from the spectral density functions of the drag force profiles. From the spectral density functions in Fig. 42, it is evident that there are either one or two significant frequencies in the drag force profile. By measuring the number of vortices shed during certain time intervals, conclusions are drawn about the relation between vortex shedding and drag force fluctuations.

In Fig. 42(a), two dominant frequencies are seen at approximately 9 Hz and 17 Hz. This is consistent for all the three depths. From the hydrogen bubble visualization, the number of vortices shed along the faces could be counted. For this purpose, the configuration with V = 200 mm/s, h = 100 mm and 100% acceleration was used. A time interval from 1.000 s to 1.143 s in the run was chosen. Figure 43 depicts the drag force profile for this chosen time interval.

Figure 44 contains snapshots of hydrogen bubble visualization at the bottom face of the flat plate. The 12 images shown in Fig. 44 cover the chosen time interval.

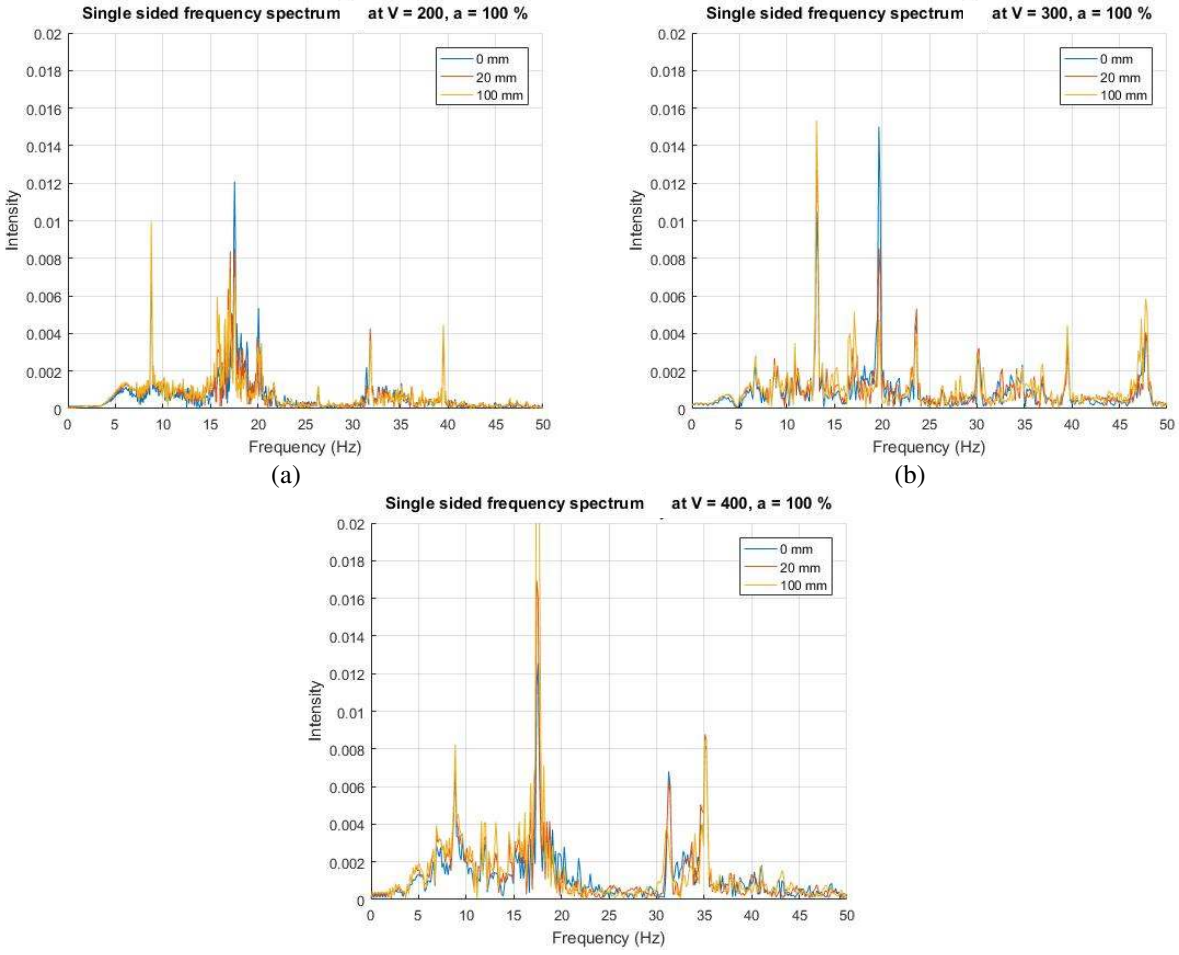

Fig. 42. Spectral density functions of drag force profiles for different depths *h,* (a) when V = 200 mm/s, (b) when V = 300 mm/s, (c) when V = 400 mm/s, at 100% acceleration.

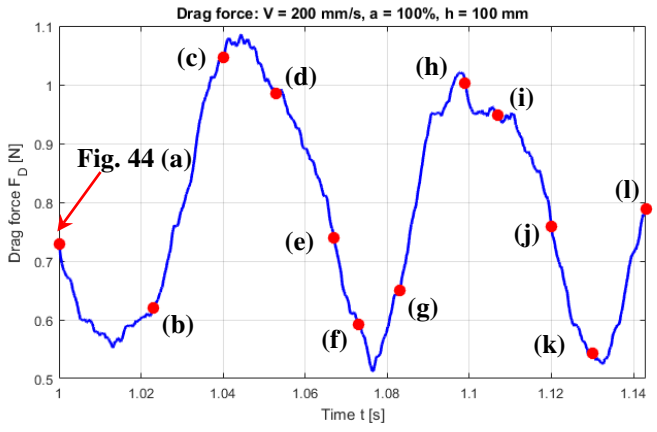

Fig. 43. Drag force profile for time interval 1 s to 1.143 s. Red dots from left to right indicate positions of the snapshots used in Fig. 44(a) to (l).

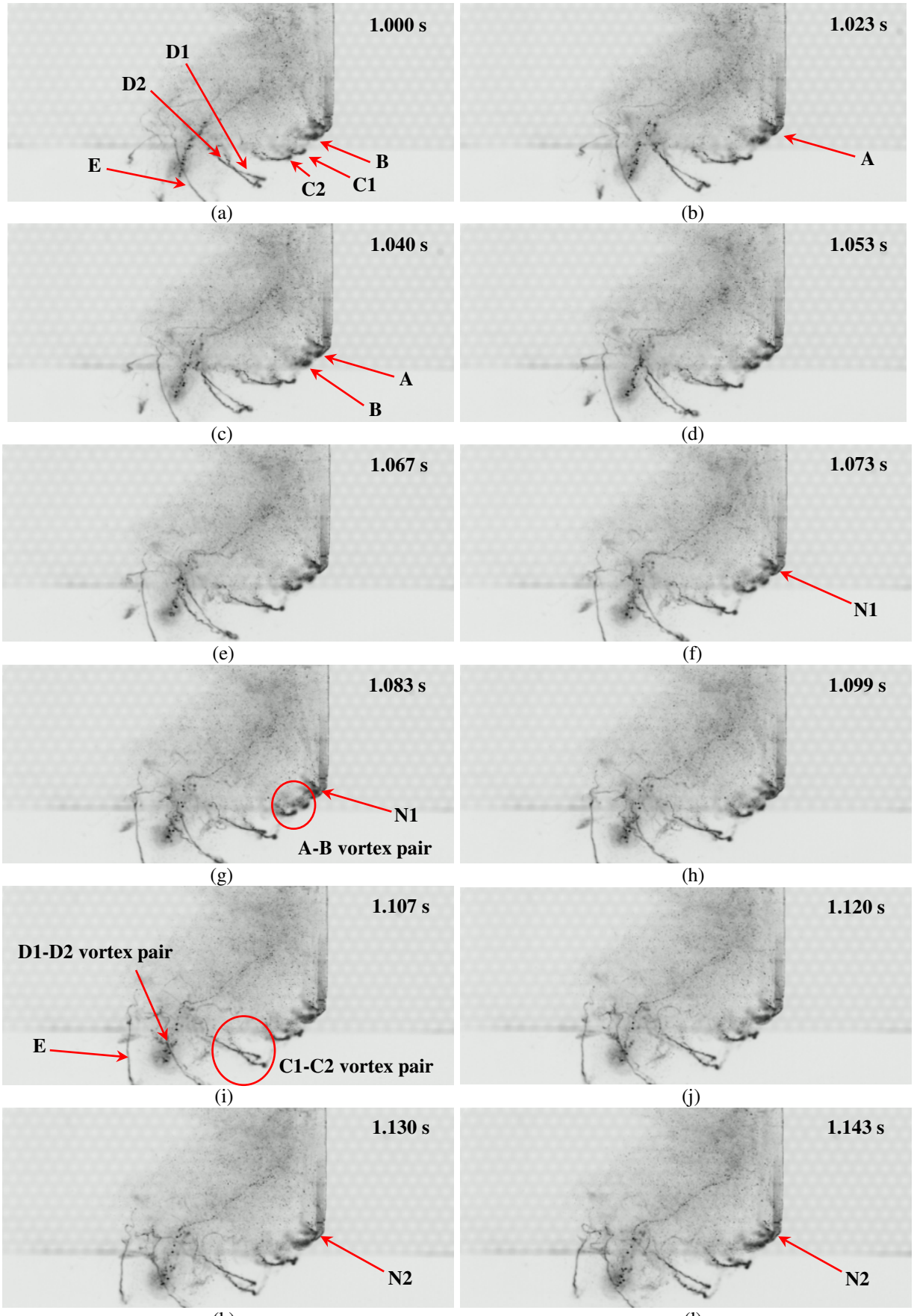

Fig. 44. Vortex shedding over the bottom face of the flat plate.

Figure 43 shows that the chosen time interval covers around 2.5 cycles of drag force fluctuations corresponding to a frequency of about 17 Hz. Figure 44(a) shows the previously shed vortices behind the bottom face of the flat plate. The recently shed vortex over the bottom face is termed as *B*. From the consecutive images, Figs. 44(b), (c), a newly formed vortex (*A*) can be seen just below the bottom face. As the vortex A detaches from the bottom face, the next vortex (*N1*) being formed is clearly seen in Figs. 44(f), (g). The time instant at which the vortex *N1* is shed coincides with a local minimum in the drag force profile, and once the *N1* vortex is shed, the drag force on the plate starts to rise. This is followed by the formation of another vortex *N2*, as shown in Figs. 44(k), (l), which decreases the drag force on the plate. The frequency of the vortex shedding cycle matches the 17 Hz dominant frequency in the drag force measurement, shown earlier in Fig. 42(a). This shows the effect of the shedding vortices on the rapid variations of the drag force of the flat plate.

From Fig. 44, another flow feature to be noted is the behavior of two consecutively shed vortices. In Fig. 44(a), a number of vortices are visible behind the bottom face of the flat plate. The vortices visible in Fig. 44(a) are: the vortex *A* forming right below the bottom face (refer 44(b)), the vortex *B* close to the bottom face, followed by two vortex pairs (*C1-C2* and *D1-D2*) and a vortex *E* which is farthest from the plate.

From Fig. 44(c), (d), there are two vortices (*A* and *B*) close to the bottom face which starts twining. The development of these twining vortices can be seen from Fig. 44(g-l). Comparing Fig. 44(i) with Fig. 44(a), it can be observed that these two vortices take on the shape of the vortex pair *C1- C2*. Also, the *C1-C2* vortex pair, as shown in Fig. 43(i) eventually evolves in the structure *D1-D2* pair, as shown in Fig. 44(a). This behavior shows that two consecutive vortices twine after shedding. This could be caused by the *pulsating bubble* (Bruno et al. [2009]) on the bottom face of the flat plate. This results in two different angles at which consecutive vortices are being shed, i.e. vortex *A* is shed at a larger angle compared to vortex *B*. Upon closer observation of the images, it was observed that vortex *A* travelled faster than vortex *B*, resulting in vortex *A* moving closer to vortex *B*. The resulting interaction between the vortex pair *A-B* caused the twining. This suggests that there exists a secondary frequency, which is caused by the oscillation of the vortex shedding angle. The effective frequency of the twining is half the vortex shedding frequency of 17 Hz, i.e. 8.5 Hz. This frequency is close to the second dominant frequency for this configuration, as shown in Fig. 42(a).

The behaviours discussed above were also observed for the remainder of the run. Similar investigations for the other configurations also confirmed that the dominant frequency in drag force was related to the vortex shedding frequencies. However, the behaviour of the twining effect was different when the frequency of the oscillation of the vortex shedding angle was not exactly half of the vortex shedding frequency. For example, in one such case, the twining effect was observed between two consecutive vortices, but every third vortex was unaffected.

3.7 PARTICLE IMAGE VELOCIMETRY

The flow visualization using hydrogen bubbles provided qualitative information on the vortex ring formation and the vortex shedding. PIV measurements are carried out in order to quantify certain features, such as the velocity field around the plate, the path of the starting vortex and the total circulation induced by the plate motion. The test cases considered are the same as mentioned in Sec. 3.4 (V = 300 mm/s, Acceleration = 100% and h = 0, 20 and 100 mm). The horizontal mid-plane of the flat plate is chosen as the measurement plane.

3.7.1 Setup parameters

A 4 Megapixel LaVision Imager Pro HS camera with a pixel size of 11 μm and a pixel format of 2016 × 2016 is used. The images are captured using a Nikon 35 mm lens with a f-stop of 5.6 and a magnification of 0.04. The images are acquired at a frame rate of 1 kHz. The velocity field is obtained by the cross-correlation of every n^{th} and $n+3^{th}$ image. The processing is done using a 32 × 32 pixel interrogation window with a 50% overlap, which gives 170 × 170 vectors for each velocity field, with a vector spacing of about 3.2 mm × 3.2 mm. The field of view is approximately 550 mm × 550 mm. This covers approximately one-third of the path during a run, when the plate moves from P1 to P2. Therefore, for a single configuration, the experiments are done thrice, covering different parts of the run, as discussed in Sec. 2.4. The velocity fields are obtained for these three individual fields of view. To obtain the velocity field for the entire run from P1 to P2, the three fields of view need to be combined. However, combining these three fields of view directly would result in an offset, both spatially and temporally. To eliminate these offsets, a stitching procedure was developed. This procedure is described in Appendix B. Additionally, from the hydrogen bubble visualization results, the size of the vortex ring and the smaller vortices are compared with the thickness of the plate. These smaller vortices are seen as streaks of hydrogen bubbles with an approximate size of one-fifth of the plate thickness. Therefore, with the current resolution of the PIV system, these smaller vortices cannot be resolved. To capture these vortices, the resolution should have been increased by an order of magnitude. However, the focus is on the dynamic behaviour of the vortex ring, which is much larger so that can be resolved easily.

Figure 45 presents the stitched velocity field at two instances (t = 1.5 s and 2.8 s) superimposed on the velocity magnitude contour. For these two time instances, the plate is at the positions x = 636 mm and 1059 mm, respectively. It can be seen in Fig. 45(a) that the velocity magnitude in the majority of the field of view is negligible except for the region surrounding the plate. However, some non-zero vectors are observed at approximately x = 1200 mm, which is where the second and third field of view are stitched. The imperfection is caused by the first PIV image of the third field of view. Since the recording was started just before the plate entered the field of view, the waves upstream, resulting from the plate movement, enter the field of view earlier than the plate. In Fig. 45(b), the impact of stitching the velocity field is visible at approximately x = 850 mm, in the form of a mismatch between the velocity magnitude contours. This mismatch can only be reduced by performing additional runs to have an improved average velocity field.

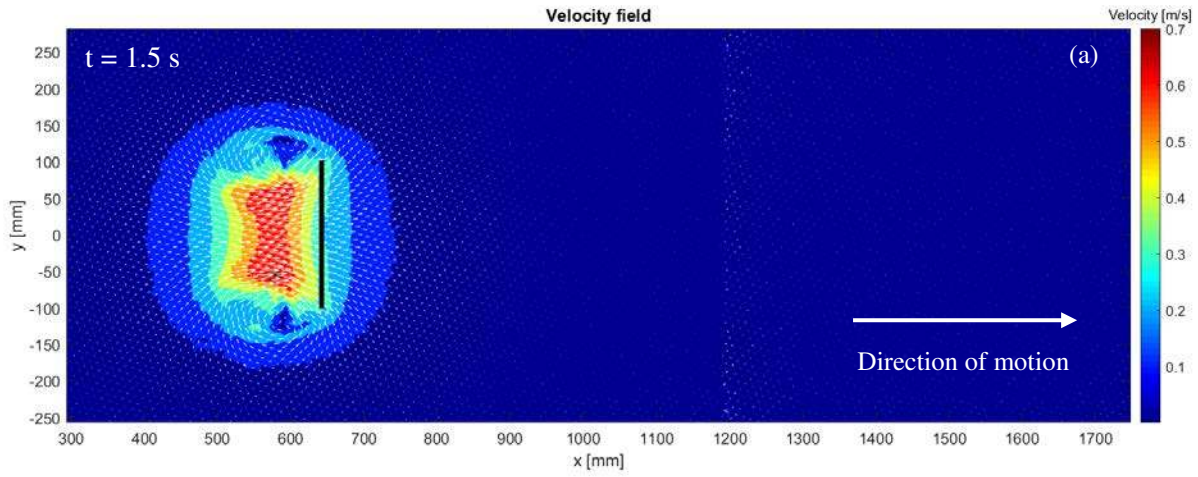

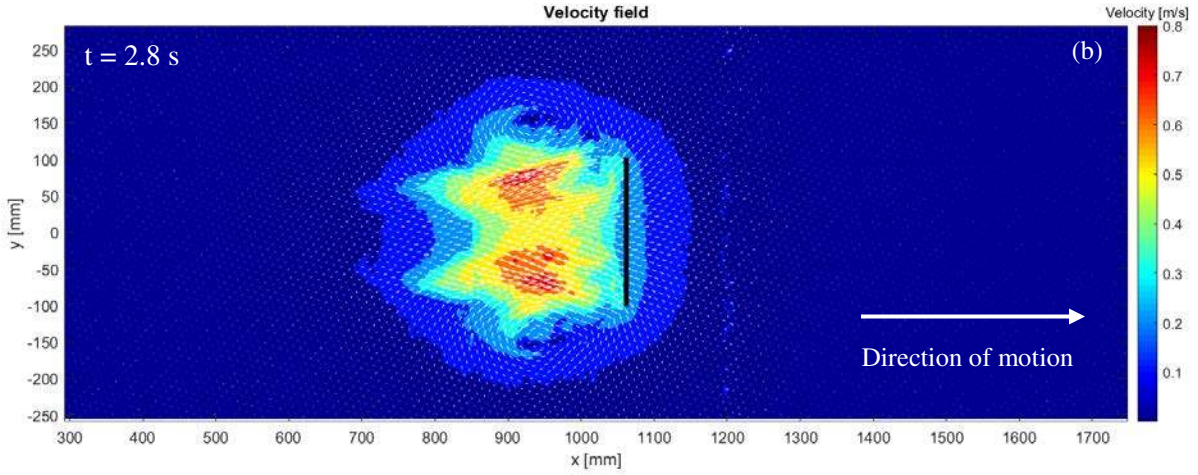

Fig. 45. Stitched velocity field covering the entire field of view. The velocity vectors are superimposed on the velocity magnitude contour. (a) When the plate is near the start (t = 1.5 s), and (b) when the plate is mid-way of the run (t = 2.8 s).

3.7.2. Comparison with hydrogen bubble visualization results

The PIV results provide the velocity fields in the horizontal mid-plane of the flat plate. The comparison of these results with the hydrogen bubble visualization images provides additional information on the flow, as this measurement plane is not entirely visible in the hydrogen bubble visualization images. Figure 46(a) shows a close up of Fig. 45(a) focusing on the velocity field in the region surrounding the plate for a depth $h = 0$ at t = 1.5 s, and Fig. 46(b) is the corresponding hydrogen bubble visualization image.

From Fig. 46(a), it can be seen that a counter-rotating vortex pair is present near the edges of the plate. From the results of the hydrogen bubble visualization in Fig. 46(b) and Sec. 3.4.2, a starting vortex is observed for this configuration. The vortex pair observed in Fig. 46(a) is a horizontal cross-section of the starting vortex. Also, a region of high velocity is observed just behind the plate. The velocity magnitude contour is found to be symmetric about $y = 0$. The smaller vortices observed in the hydrogen bubble visualization images are not captured with the current PIV system because of the low spatial resolution, as was mentioned before.

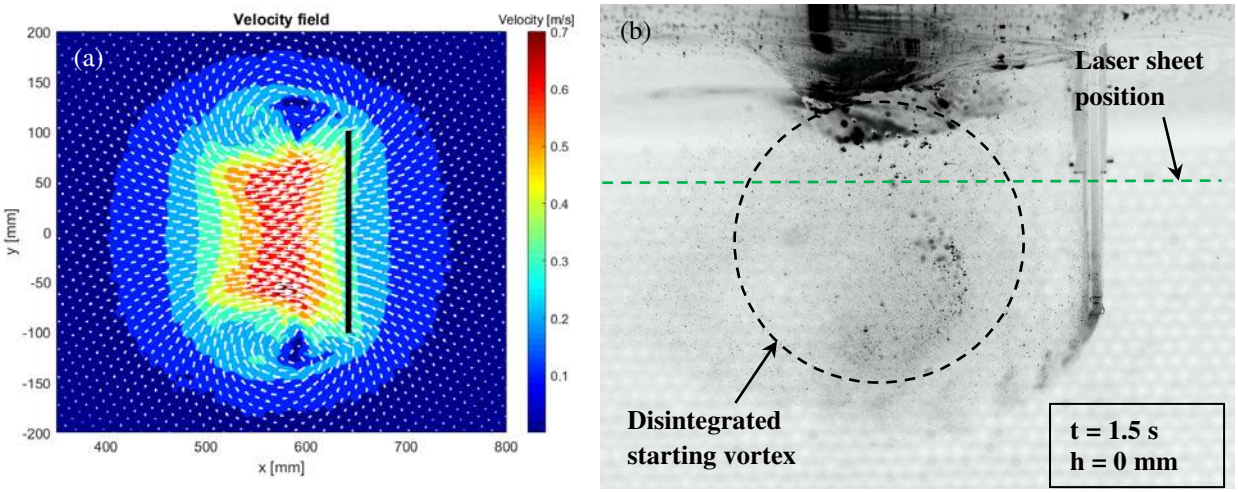

Fig. 46. (a) Velocity vectors superimposed on the velocity contour magnitude for the $h = 0$ mm case and (b) Corresponding hydrogen bubble visualization image.

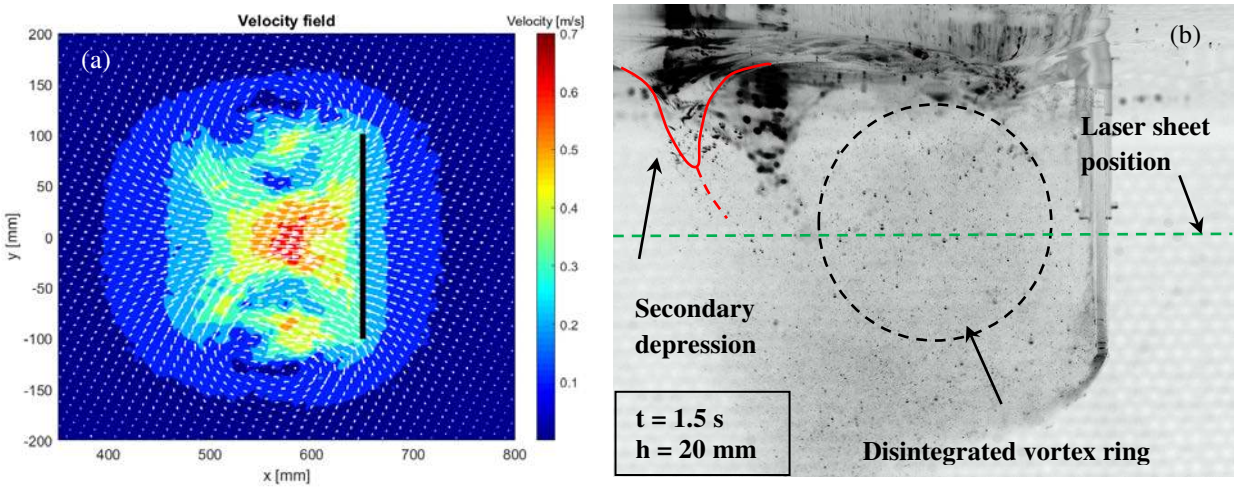

Fig. 47. (a) Velocity vectors superimposed on the velocity contour magnitude for the h = 20 mm case and (b) Corresponding hydrogen bubble visualization image.

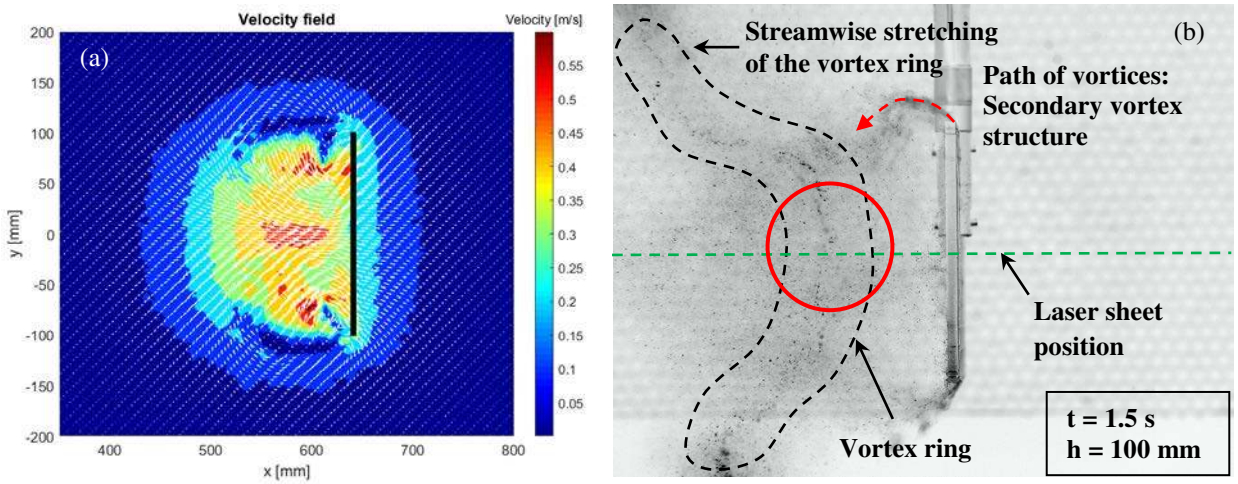

Fig. 48. (a) Velocity vectors superimposed on the velocity contour magnitude for the h = 100 mm case and (b) Corresponding hydrogen bubble visualization image.

A similar analysis for the other cases (h = 20 mm and 100 mm) provides additional information on the flow. Figures 47(a) and 48(a) show the velocity vectors superimposed on the velocity magnitude contour at t = 1.5 s for the h = 20 mm and the 100 mm cases, respectively. Comparing Figs. 46(a), 47(a) and 48(a), differences in the velocity fields at the different plate depths can be clearly seen. The analysis of the hydrogen bubble visualization images in Sec. 3.4 also indicated major differences in flow behaviour when the depth h was changed. Figures 47(b) and 48(b) show the hydrogen bubble visualization images corresponding to Figs. 47(a) and Fig. 48(a) respectively.

The flow behaviour observed are similar to the earlier observations made using hydrogen bubble visualization. From Fig. 47(b) and the discussion of phase B for the h = 20 mm case in Sec. 3.4.2, it is evident that there exists a disintegrated vortex ring behind the plate. Further downstream, two depressions in the air-water interface are observed, one of which is highlighted in Fig. 47(b). These depressions form a counter-rotating vortex pair. The strength of these vortices cause water to circulate around the red dotted line shown in Fig. 47(b). Hence, it can be expected that there is a low velocity region at this location, which is approximately at a distance of one plate width behind the flat plate. In Fig. 47(a), this can be seen at approximately x = 550 mm and y = ± 60 mm, where two low velocity regions are observed. For the h = 100 mm case in Fig. 47(a), it can be seen that there are two low velocity regions directly behind the plate at approximately x = 620 mm and y = ± 90 mm. Figure 48(b)

and the discussion of phase B for the h = 100 mm case in Sec. 3.4.1 show that at this time instant, the part of the vortex ring near the laser sheet position (indicated by a red circle in Fig. 48(b)) is closer to the plate. However, the distance between the front and back portions of the vortex ring cannot be determined from the hydrogen bubble visualization images. Fig. 48(a) shows that these low velocity regions close to the plate at approximately x = 620 mm could be the location of the front and back portions of the vortex ring. An additional analysis is thus required to support this claim. This is done by tracking the vortex ring from the start of the plate motion, as will be discussed below.

3.7.3. Tracking the starting vortex

The identification of the vortices from the velocity fields obtained from PIV results give quantitative information on the movement of the starting vortex, which includes both the U-shaped starting vortex and the vortex ring that was discussed in Sec. 3.4. In the current PIV measurement, a horizontal cross-section of the starting vortex at the mid-plane of the plate is observed. By tracking the starting vortex core in a plane which is not well distinguished during the hydrogen bubble visualization technique, further quantitative information on the dynamics of the starting vortex is obtained.

The tracking of the starting vortex is performed by determining the local swirling strength of the instantaneous velocity fields. The local swirling strength is quantified as the imaginary part of the complex eigenvalues of the velocity gradient tensor (Zhou et al. [1999]). Therefore, by calculating the velocity gradient tensor at each data point in the velocity field, the local swirling strength is determined. It should be noted that the velocity field was filtered (by using a *hampel filter*) before determining the velocity gradient tensor to reduce the effects of the noise in the velocity field. Also, only the velocity fields for the first field of view are used. The instantaneous velocity fields from the other two fields of view are not used because the starting vortex disintegrates by the time it reaches the second field of view. Figure 49 shows the contour plot of the swirling strength at time t = 1.7 s for the h = 0 mm case. It can be seen that there are two regions with strong swirling strength close behind the plate. These regions correspond to the starting vortex. Assuming the maximum swirling strength is present within the starting vortex, the swirling strength contour plot is used to track the position of the starting vortex.

For the three cases (h = 0, 20 mm and 100 mm), the location of the data point with the maximum swirling strength is identified up to t = 2 s. After this time instant, both the plate and the disintegrated starting vortex would have reached the second field of view.

In the horizontal cross section (at the mid-plane of the plate) of the starting vortex, there are two vortices which are called *top* and *bottom* vortex, see Fig. 49. Figure 50 shows the x and y coordinates of these two vortices as a function of time for the h = 0 mm case. The position of the plate and the magnitude of the maximum swirling strength are also plotted as a function of time. The following observations can be made from Fig. 50:

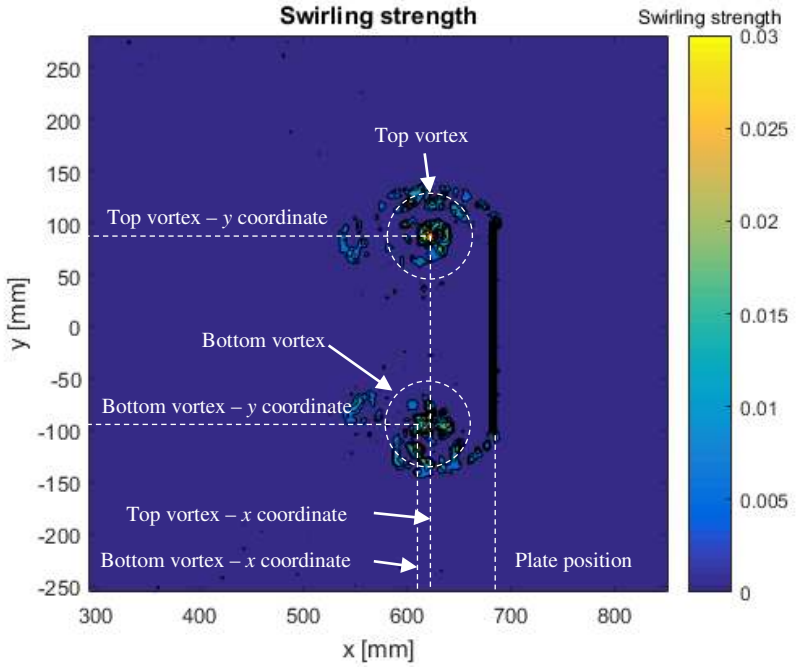

Fig. 49. Swirling strength contour in the first field of view.

- The erratic fluctuations of the *x* and *y* coordinates of the two vortices at the start of the run is due to the fact that the starting vortex is not identifiable until approximately t = 0.22 s. Before that time, the starting vortex is too small to be resolved by the current PIV system.
- After approximately t = 0.22 s, a clear maximum in swirling strength is identifiable in each instantaneous velocity field and the location of the starting vortex is captured from the PIV results. This is accompanied by an increasing swirling strength maximum.
- In the later stages, the *x* and *y* coordinates start to fluctuate accompanied by a decrease in the swirling strength maxima, suggesting that the starting vortex is collapsing.
- By comparing the plate position with the *x*-coordinate of the vortices, the distance of these vortices behind the plate can be determined. By comparing the two *y*-coordinates, the distance between the two vortices can be determined.

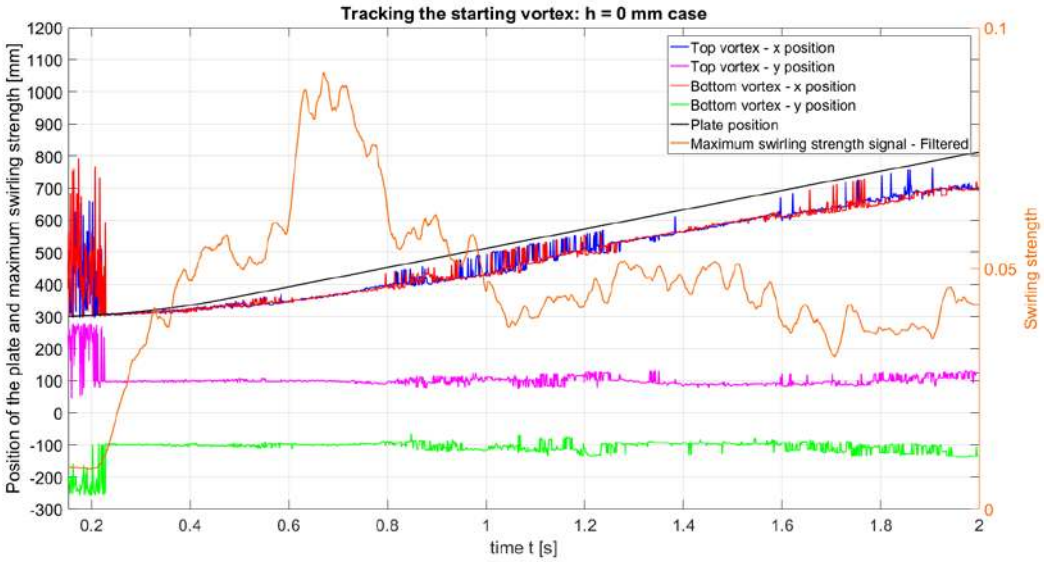

Fig. 50. Tracking the starting vortex using swirling strength for *h* = 0 mm case.

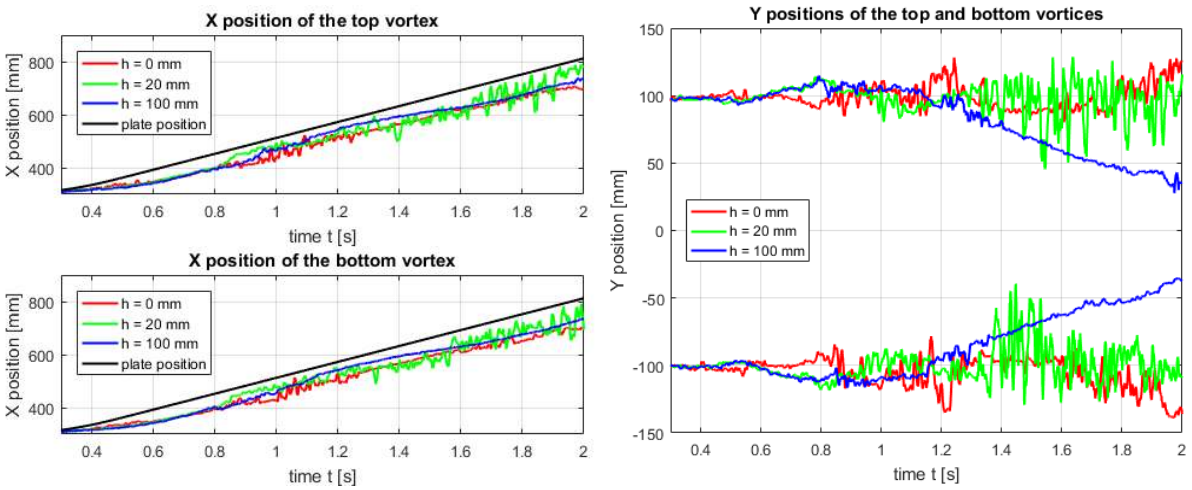

Fig. 51. (a) x-coordinates of the two vortices, (b) y-coordinates of the two vortices.

Figures 51(a) and (b) present the x and y coordinates of the two vortices for the three cases (h = 0, 20 mm and 100 mm). The following case specific observations can be made from Fig. 51.

- A comparison of the x coordinates of the two vortices with the plate position in Fig. 50(a) shows that the gap between the x-coordinates of the vortices and the plate position is increasing very slowly, suggesting that the vortex pair is not detaching from the immediate wake but moving along with the plate for all three cases.
- For the h = 20 mm case, the extreme fluctuations in the x and y coordinates between 0.8 s and 1.2 s suggest that the starting vortex is temporarily not well identifiable due to a reduction of the swirling strength. This suggests a temporary disturbance to the starting vortex.
- For the h = 0 case, it is observed that the gap between the y coordinates increase, which shows that the vortices are diverging. For the h = 20 mm case, the magnitude of the fluctuation of the x and y coordinates after 0.8 s starts increasing. This suggests that the starting vortex has completely disintegrated.
- For the h = 100 mm case, the fluctuations of the coordinates are comparatively lower than the other cases. This suggests that the starting vortex (vortex ring in this case) is highly stable. Also, the gap between the y positions starts reducing as time progresses, which shows that the vortices are moving closer to each other. This spanwise contraction is a different behaviour when compared to the other parts of the vortex ring (streamwise stretching, as observed in Fig. 48(b) and Sec. 3.4.1). Therefore, this supports the claim made for the h = 100 mm case in Sec. 3.7.2., where the low velocity regions close behind the plate were suggested to be caused by the vortex ring.

To summarize, the analysis using the local swirling strength provided information on the movement of the starting vortex, and also showed whether the starting vortex has disintegrated. The analysis also provided additional information on the behaviour of the vortex ring in the h = 100 mm case, which could not be determined from the hydrogen bubble visualization results.

3.7.4. Total circulation in the measurement plane

The swirling strength analysis provided details on the movement of the starting vortex and an indication of when the starting vortex may have collapsed. The total circulation on the measurement plane is used to determine the flow behaviour. Figure 52 shows the total circulation in the measurement plane for the three configurations considered.

The total circulation in the measurement plane was determined from:

$$\Gamma = \iint_S \omega \, . \, d\boldsymbol{S}$$

where ω is the vorticity and S represents the surface area of the measurement plane. The vorticity ω was calculated from the velocity gradients at each grid point using the central differencing scheme. The vorticity obtained for each grid point is then multiplied by its cell area giving the circulation for each cell. The summation of these values provides the total circulation in the measurement plane. Also, it should be noted that the total circulation Γ was calculated for the entire field of view for the entire run. The total circulation Γ as a function of time is shown in Fig. 52.

- With increase in time, the total circulation generally increases. The magnitude of the total circulation increases with increase in depth. As the depth h increases, the formation of the vortex ring is undisturbed and is expected to have a stronger vorticity. This could have resulted in a higher total circulation with an increase in depth.
- However, after t = 4 s, it can be seen that for the h = 20 mm case, the total circulation is higher compared to the h = 100 mm case. This could be due to the compact wake in the h = 20 mm case, as discussed in Sec. 3.4.2.
- In the h = 20 mm case, it can be observed that there are a few minor dips near t = 1 s. From the previous analysis in Sec. 3.7.3., it was seen that the starting vortex collapses near this time instant. This collapse could have caused the minor dips in the total circulation.
- Another observation is that, in the h = 0 mm case, a dip in the total circulation can be observed after t = 0.6 s. Figure 53 and Sec. 3.4.2 show that an interaction between a cloud and the starting vortex results in the disintegration of the latter. Figure 53(d) shows that the collapse is visible after t = 0.8 s, but the total circulation starts dropping at approximately t = 0.6 s. This could be explained by the cloud of hydrogen bubbles moving downwards behind the plate. This cloud has a clockwise rotation when viewed from the front, which causes out of plane motion in the chosen measurement plane, which in turn affects the total circulation. This sequence of events is thus responsible for the dip in total circulation after t = 0.6 s and the collapse of the starting vortex happening later at t = 0.8 s, as suggested in Sec. 3.7.3.

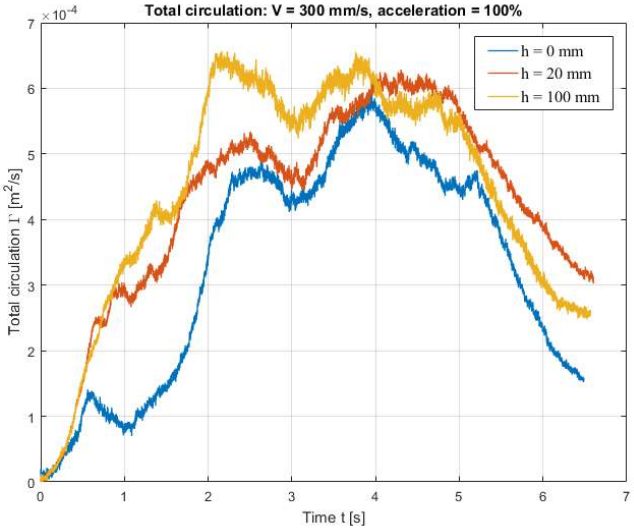

Fig. 52. Total circulation at different depths in the chosen measurement plane.

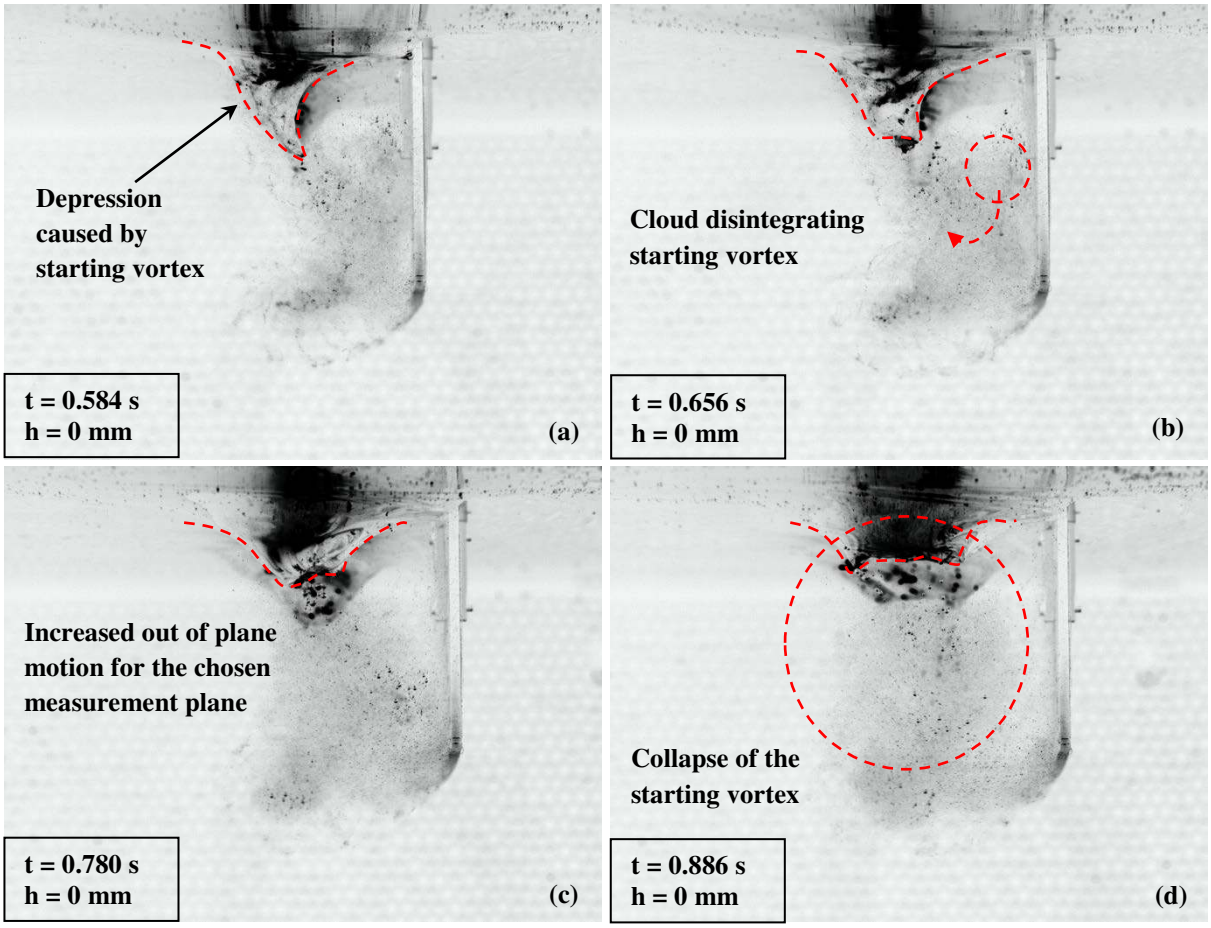

Fig. 53. Hydrogen bubble visualization images capturing the reason for the dip in total circulation in the h = 0 mm case.

Similar comparisons between the hydrogen bubble visualization results and the total circulation could be used to determine the reason behind the other major dips that occur in the total circulation profile.

Using Particle Image Velocimetry the velocity fields determined in the horizontal mid-plane of the plate showed the effect of the starting vortex in the wake. The comparison of the PIV results with the hydrogen bubble visualization showed good agreement in terms of the position of the starting vortex. PIV also revealed the spanwise contracting behaviour of the vortex ring, which was not well distinguished in the hydrogen bubble visualization. The local swirling strength and the total circulation on the measurement plane indicated the location of the starting vortex and the changes in the flow. However, it is insufficient to provide a complete description of the flow behaviour compared to the hydrogen bubble visualization. With additional measurement planes and a higher spatial resolution, the results would be sufficient to fully resolve the flow.

4

CONCLUSIONS

An experimental work to study the effect of the depth of a flat plate below the air-water interface was performed at the Laboratory for Aero and Hydrodynamics of TU Delft. The experiments were carried out using a 4-axes industrial robot, a large water tank, a PIV system and a hydrogen bubble visualization setup.

The linear translation of the flat plate through the water was achieved by attaching it to the head of a 4-axis industrial robot and a water tank. The robot and a force/torque transducer that connects the robot head and the plate provide data regarding the position and the velocity of the plate and the force/torque acting on it. Using this data, the drag force acting on the flat plate was determined as a function of time.

The drag force profile was divided into three phases: acceleration, transition and steady phase. The acceleration phase was characterized by a strong increase in the drag force due to the added mass effect and a force computed from the steady phase drag coefficient. The transition phase was characterized by a decay of the drag force which was found to be strongly dependent on the plate depth h. The steady phase was characterized by a steady drag force dependent on the square of the plate velocity. High frequency oscillations of the drag force were noticeable throughout the three phases.

Extensive analysis on the effect of the air-water interface on the drag force profile led to the identification of the depth h at which the drag force on the plate was at its maximum. This high drag case was found to be at h = 20 mm. The comparison of this case to the other considered cases (h = 0 and h = 100 mm) led to the determination of the behavioural changes of the drag force, as the plate depth h increases. The drag force behaviour was found to be similar in the acceleration and the steady phases, with the only noticeable difference in the magnitude of the drag force. However, during the transition phase, the drag force behaviour showed significant differences between the three cases. In the h = 100 mm case, secondary peaks (peak 1 and peak 2) in the drag force behaviour were observed, which were barely visible in the other cases. To identify the source of this different behaviour, hydrogen bubble visualization technique was used.

The hydrogen bubble visualization for the h = 100 mm case showed the presence of a vortex ring being formed during the acceleration phase. The formation and development of this vortex ring affects the drag force and is correlated to peak 1 in the drag force profile. The disintegration of the vortex ring leads to the formation of the secondary vortex structure, which was responsible for the peak 2 in the drag force profile. As time progressed, the influence of the remnants of the vortex ring became negligible, and the plate entered the steady phase. For the h = 0 mm case, the formation of the vortex ring was prevented because of the air-water interface, resulting in a different drag force behaviour. Instead, a U-shaped starting vortex was formed which disintegrated rather quickly resulting in a decreased influence on the plate. As a result, the secondary peaks in the drag force profile were relatively weaker. In both these cases, a wide wake was observed during the steady phase. For the h = 20 mm case, a vortex ring was formed during the acceleration phase. However, the

narrow gap between the plate and the air-water interface restricted the development of the vortex ring, resulting in the streamwise stretching of the vortex ring. The reason for the high drag during this case was due to the formation of the compact wake behind the top face of the plate resulting in a low pressure region.

The results of the hydrogen bubble visualization were used to determine the correlation between the flow behaviour and the overall drag force behaviour. A close inspection of the shedding of small vortices at the edges of the plate gave insights into the high frequency fluctuations of the drag force. It was found that one of the dominant frequencies correlated with the vortex shedding frequency. The behaviour of the subsequent vortices showed a twining effect which led to the conclusion that the secondary dominant frequency was a consequence of the oscillation of the vortex shedding angle.

A correlation of the physical features with the drag force behaviour was determined. However, the drag force profile did not agree with the theoretical expectation. Therefore, an extensive decomposition of the drag force profile was performed, followed by an attempt towards the development of a drag force model. This led to the identification of the two additional forces F_{AM} and F_{DECAY}. The force F_{AM} showed that the added mass effect was no longer a constant, but time dependent. This force was attributed to the developing starting vortex, which was believed to influence the effective geometry of the plate. As the size and the strength of the starting vortex increased, this force F_{AM} also increased. On the other hand, the force F_{DECAY} was attributed to the decay of the starting vortex, which still has an influence over the drag force on the plate. Therefore, instead of an instantaneous decrease in the drag force, a gradual decay was observed.

Particle Image Velocimetry (PIV) measurements has been performed in the horizontal mid-plane of the flat plate. The velocity fields thus obtained provided a quantitative insight on the counter rotating vortex pair and the high velocity regions behind the plate. The tracking of the starting vortex position was performed using the local swirling strength from t = 0 up to t = 2 s. For the h = 0 mm case, the starting vortex was temporarily disturbed as evidenced from a temporary decrease in swirling strength, however the position of the vortex pair with respect to the plate remained relatively unchanged during the chosen time interval. For the h = 20 mm case, it was observed that the starting vortex disintegrated completely after t = 0.8 s. For the h = 100 mm case, the starting vortex remained stable during the entire interval. A significant difference between the h = 100 mm and the other two cases was that the counter rotating vortex pair was moving closer to each other, in contrast to the streamwise stretching at the other parts as observed in the hydrogen bubble visualization results. An analysis on the total circulation on the measurement plane provided information on the disintegration of the starting vortex. For the h = 0 mm case, a dip in the total circulation after t = 0.6 s was observed, which was attributed to the collapse of the starting vortex and increased out of plane motion as observed from hydrogen bubble visualization.

BIBLIOGRAPHY

[1] Baudouin, A. & Hawkins, D. (2002). A biomechanical review of factors affecting rowing performance, British Journal of Sports Medicine, 36, 396-402.

[2] Scragg, C.A. & Nelson, B.D. (1993). The design of an Eight-Oared Rowing Shell, Marine Technology, 30(2), 84-99.

[3] Mola, A., Formaggia, L. & Miglio, E. (2006). Simulation of the dynamics of an Olympic rowing boat, Proceedings of European Conference on Computational Fluid Dynamics ECCOMAS CFD 2006.

[4] Zhang, D. & Zheng, W. (2011). International Development of the Research on the Hydrodynamic Performance of Rowing, 2011 International Conference on Future Computer Science and Education (ICFCSE).

[5] Day, A.H., Campbell, I., Clelland, D. & Cichowicz, J. (2011). An experimental study of unsteady hydrodynamics of a single scull, Proceedings of the Institution of Mechanical Engineers, Part M: Journal of Engineering for the Maritime Environment, 225(3), 282-294.

[6] Formaggia, L., Miglio, E., Mola, A. & Montano, A. (2008). A model for the dynamics of rowing boats, International Journal for Numerical Methods in Fluids, 61. . 10.1002/fld.1940.

[7] Formaggia, L., Miglio, E., Mola, A. & Parolini, N. (2008). Fluid-structure interaction problems in free surface flows: Application to boat dynamics, International Journal for Numerical Methods in Fluids, 56, 965-978.

[8] FISA Rule Book, 2017. http://www.worldrowing.com/fisa/publications/rule-book.

[9] Kleshnev, V. (1999). Propulsive efficiency of rowing, Scientific Proceedings: ISBS '99: XVII International Symposium on Biomechanics in Sports, 69–72. Perth, WA: School of Biomedical and Sports Science, Edith Cowan University.

[10] Sliasas, A. & Tullis, S. (2009). Numerical modelling of rowing blade hydrodynamics, Sports Engineering, 12, 31-40.

[11] Pulman, C. (2005). The Physics of Rowing, University of Cambridge.

[12] Leroyer, A., Barre, S., Kobus, J.M. & Visonneau, M. (2010). Influence of free surface, unsteadiness and viscous effects on oar blade hydrodynamic loads, Journal of Sports Sciences, 28(12), 1287-1298.

[13] Caplan, N., & Gardner, T.N. (2007). Optimization of oar blade design for improved performance in rowing, Journal of Sports Sciences, 25(13), 1471-1478.

[14] Caplan, N., & Gardner, T.N. (2007). A fluid dynamic investigation of the Big Blade and Macon oar blade designs in rowing propulsion, Journal of Sports Sciences, 25(6), 643-650.

[15] Coppel, A., Gardner, T.N., Caplan, N. & Hargreaves, D.M. (2009). Simulating the fluid dynamic behaviour of oar blades in competition rowing, Journal of Sports Engineering and Technology, 224, 25-35.

[16] Taneda, S. & Honji, H. (1971). Unsteady Flow past a Flat Plate Normal to the Direction of Motion, Journal of the Physical Society of Japan, 30(1), 262-272.

[17] Leroyer, A., Barre, S., Kobus, J.M. & Visonneau, M. (2008). Experimental and numerical investigations of the flow around an oar blade, Journal of Marine Science and Technology, 13, 1-15.

[18] Tonui, N. & Sumner, D. (2011). Flow around impulsively started square prisms, Journal of Fluids and Structures, 27, 62-75.

[19] Gharib, M. & Kim, D. (2011). Characteristics of vortex formation and thrust performance in drag-based paddling propulsion, The Journal of Experimental Biology, 214, 2283-2291.

[20] Tian, X., Ong, M.C., Yang, J. & Myrhaug, D. (2014). Large-eddy simulation of the flow normal to a flat plate including corner effects at a high Reynolds number, Journal of Fluids and Structures, 49, 149-169.

[21] Kiya, M. & Sasaki, K. (1983). Structure of a turbulent separation bubble, Journal of Fluid Mechanics, 137, 83-113.

[22] Iio, S., Takahashi, K., Haneda, Y. & Ikeda, T. (2008). Flow Visualization of Vortex Structure in a Pulsed Rectangular Jet, Journal of Visualization, 11, 2:125-132.

[23] Morton, C. & Yarusevych, S. (2015). Three-dimensional flow and surface visualization using hydrogen bubble technique, Journal of Visualization, 18, 47-58.

[24] Sabatino, D. R., Praisner, T.J., Smith, C.R. & Seal, C.V. (2012). Hydrogen Bubble Flow Visualization, Book: Flow Visualization: Techniques and Examples, Publisher: Imperial College Press, London, Chapter 2, 19.

[25] Bruno, L., Coste, N. & Fransos, D. (2009). Analysis of the separated flow around a 5:1 rectangular cylinder through computational simulation, Proceedings of 5th European and African Conference on Wind Engineering, EACWE 5.

[26] Pullin, D.I. & Perry, A.E. (1980). Some flow visualization experiments on the starting vortex, Journal of Fluid Mechanics, 97(2), 239-255.

[27] Ringuette, J., Milano, M. & Gharib, M. (2007). Role of the tip vortex in the force generation of low-aspect-ratio normal flat plates, Journal of Fluid Mechanics, 581, 453-468.

[28] Yu, Yee-Tak (1945). Virtual Masses of Rectangular Plates and Parallelepipeds in Water, Journal of Applied Physics, 16, 724.

[29] Patton, K. (1965). An Experimental Determination of Hydrodynamic Masses and Mechanical Impedances, USL Report No. 677.

[30] Jacobs, A.F.G. (1985). The normal-force coefficient of a thin closed fence, Boundary-Layer Meteorology, 32(4), 329-335.

[31] Bearman, P. (1971). An investigation of the forces on flat plates normal to a turbulent flow, Journal of Fluid Mechanics, 46(1), 177-198.

[32] Ortiz, X., Rival, D. & Wood, D. (2015). Forces and Moments on Flat Plates of Small Aspect Ratio with Application to PV Wind Loads and Small Wind Turbine Blades, Energies, 8(4), 2438-2453.

[33] Gharib, M., Rambod, E. & Shariff, K. (1998). A universal time scale for vortex ring formation, Journal of Fluid Mechanics, 360, 121-140.

[34] Zhou, J., Adrian, R.J., Balachandar, S. & Kendall, T.M. (1999). Mechanisms for generating coherent packets of hairpin vortices in channel flow, Journal of Fluid Mechanics, 387, 353-396.

APPENDIX A

A.1 Effect of hydrogen bubble visualization on drag force measurement

From the results in Fig. 26 and 27, it is clear that there are significant differences in the drag force acting on the plate for different h values. To understand the cause of these differences, the flow around the plate was visualized using the Hydrogen bubble technique. Before considering the results of the visualization, it is first investigated whether the hydrogen bubbles have an effect on the flow field and thus on the measured drag force value. This section determines the effect of inclusion of the hydrogen bubbles and the addition of a cathode on the surface of the plate.

To determine the effect of adding hydrogen bubbles to the flow, a comparison was made between the drag force profiles for two runs (with and without hydrogen bubbles) for the configuration with h = 100 mm, V = 300 mm/s and 100% acceleration. The drag force profiles for these two runs are depicted in Fig. A1 and A2. Figure A1 shows that the overall drag force profile is preserved predominantly, including the initial peak and the two secondary peaks. Part of the data shown in Fig. A1, highlighted by the black rectangle, is zoomed in to depict this difference, as shown in Fig. A2. The profile of these fluctuations remain consistent between the two runs, but there exists minor differences in the magnitude.

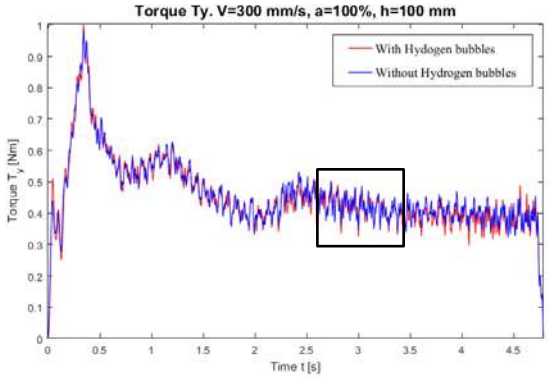

Fig. A1. Effect of hydrogen bubbles on drag force on flat plate.

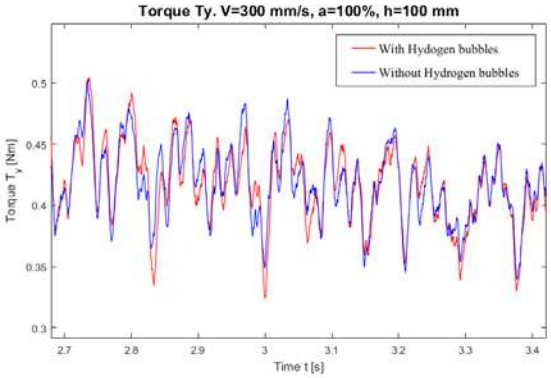

Fig. A2. Effect of hydrogen bubbles within a small time interval.

To determine the effect of inclusion of hydrogen bubbles and the addition of the cathode on the surface of the plate, the following factors were calculated:

$$X_t = \left(\frac{Drag\ force_{t,\ with\ hydrogen} - Drag\ force_{t,\ without\ hydrogen}}{Drag\ force_{t,\ without\ hydrogen}}\right) * 100\%$$

$$Y_t = \left(\frac{Drag\ force_{t,run\ 2\ without\ HBV\ setup} - Drag\ force_{t,run\ 1\ without\ HBV\ setup}}{Drag\ force_{t,run1\ without\ Hydrogen\ Bubble\ Visualization\ (HBV)\ setup}}\right) * 100\%$$

$$Z_t = \left(\frac{Drag\ force_{t,run\ with\ hydrogen} - Drag\ force_{t,run\ without\ HBV\ setup}}{Drag\ force_{t,run\ without\ Hydrogen\ Bubble\ Visualization\ (HBV)\ setup}}\right) * 100\%$$

Where, t = 0.1 s to 4.7 s in steps of 1e-4 s, X is the percentage increase due to the inclusion of hydrogen bubbles, Y is the percentage increase between two identical runs without the Hydrogen bubble visualization setup and Z is the percentage increase between two identical runs: with hydrogen bubbles and without the Hydrogen bubble visualization setup.

h (mm)	Mean(*X*) (%)	Standard deviation(*X*) (%)
0	0.21	5.43
20	0.93	3.74
100	1.16	4.28

Table A1. Mean and Standard deviation of X for different *h* values.

h (mm)	Mean(*Y*) (%)	Standard deviation(*Y*) (%)
0	0.53	4.99
20	1.88	4.71
100	1.15	4.57

Table A2. Mean and Standard deviation of Y for different *h* values.

h (mm)	Mean(*Z*) (%)	Standard deviation(*Z*) (%)
0	1.98	6.12
20	1.09	4.09
100	2.63	4.72

Table A3. Mean and Standard deviation of Z for different *h* values.

Table A1 lists the percentage increase in the drag force measurements due to the addition of hydrogen bubbles and Table A2 lists the percentage increase between two identical runs with no cathode wires on the surface of the plate. It is observed that the deviation of X is less than the deviation observed in Y. This shows that the addition of hydrogen bubbles is indiscernible in its effect in the drag force measurement.

Table A3 lists the percentage increase in the drag force measurements due to the addition of the cathode wire and hydrogen bubbles. Comparing these values with Table A1 and A2 suggest that the addition of cathode and hydrogen bubbles increase the mean and standard deviation by approximately 1.5%.

A.2 Repeatability of drag force measurement during Hydrogen bubble visualization

Similar to determining the effect of hydrogen bubbles on drag force, it was necessary to determine the repeatability of the drag force measurement during the Hydrogen bubble visualization technique. Therefore, two runs with h = 0 mm (V = 300 mm/s and 100% acceleration) are compared, in Fig A3. Figure A3 depicts only a portion of the run, because the overall drag force profile was similar. It can be observed from Fig. A3, that the profile of the fluctuations remain consistent between the two runs, but there exists minor differences in magnitude. Calculation of Q for these two runs yielded a mean of 1.46% with a standard deviation of 4.77%. Comparing with the values presented in Sec. A.1, it is observed that the deviation between two identical hydrogen bubble runs is within the limits of measurement uncertainty.

$$Q_t = \left(\frac{Drag\ force_{t,run2\ with\ hydrogen} - Drag\ force_{t,run1\ with\ hydrogen}}{Drag\ force_{t,run1\ with\ hydrogen}} \right) * 100\%$$

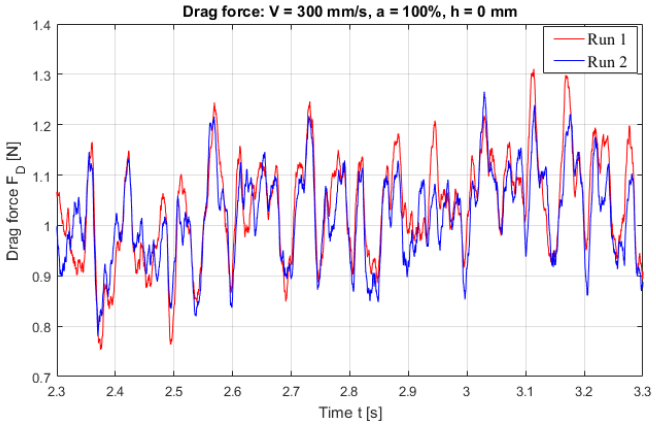

Fig. A3. Repeatability of Hydrogen bubble visualization runs.

A.3 Repeatability of Hydrogen bubble visualization

Figure A4 depicts two time instances from the two separate runs discussed in Fig. A3 (V = 300 mm/s and 100% acceleration, h = 0 mm). In terms of visualization, comparing the hydrogen bubble positions inside the red circles in Fig. A3, the visible differences are minute. The structure of the starting vortex and the air-water interface depressions look similar between the two cases. Moreover, these two runs were performed a few days apart. This indicated good repeatability of hydrogen bubble visualization over time, in the current work.

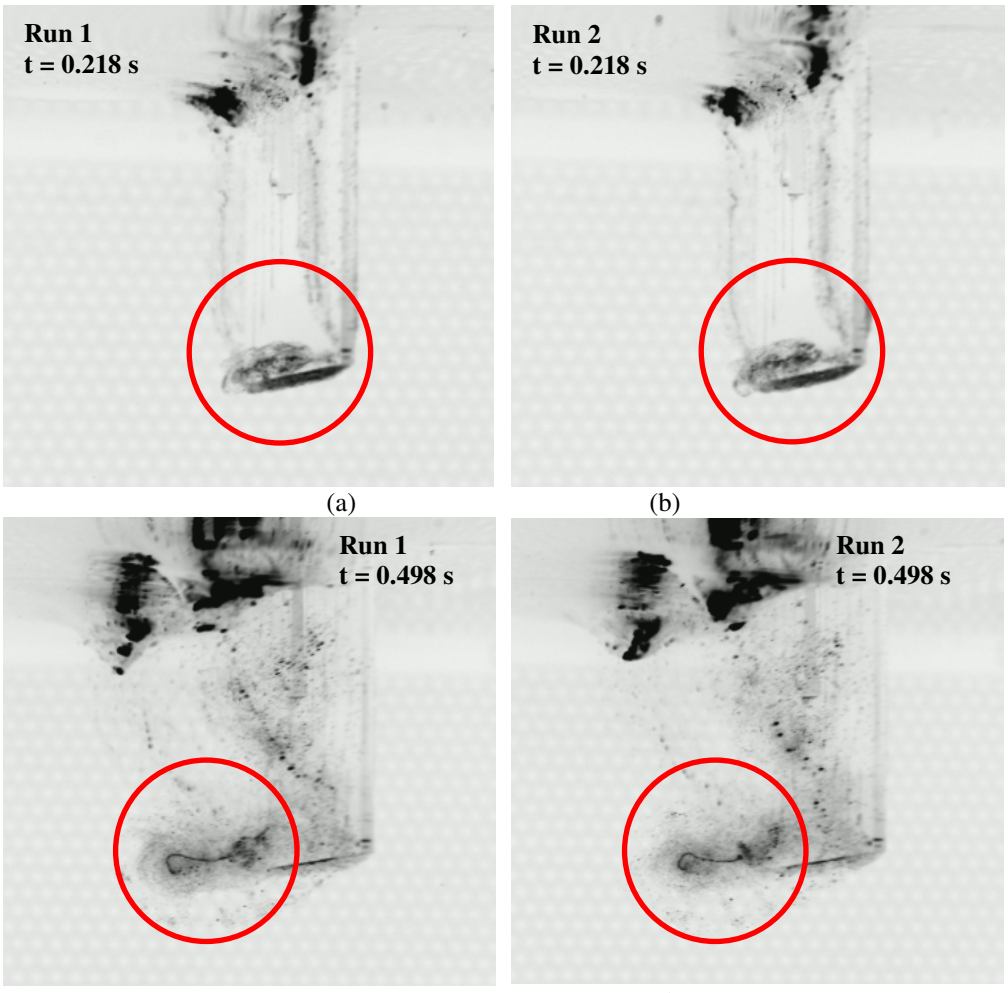

Fig. A4. Repeatability of Hydrogen bubble visualization within two identical runs, (a), (b) snapshots from phase A and (c), (d) snapshots from phase B.

APPENDIX B

B.1 Stitching the velocity fields to obtain the desired field of view

During particle image velocimetry, the field of view was not sufficient to capture the entire run. Therefore, to capture the run, the desired field of view was split into three sections, as discussed in Sec. 2.4. These sections were stitched together, which allows investigation of the entire plane. However, to obtain the field of view for the entire run, combining these individual fields of view directly would result in an offset, both spatially and temporally. Therefore, it was necessary to eliminate these offsets with the following adjustments.

i. Before the start of each experiment, calibration was done. The three fields of view for a single run are shown in Fig. B1. The centers of the calibration plate (C_1, C_2 and C_3) given by the robot, were used as the reference points in the stitching process.

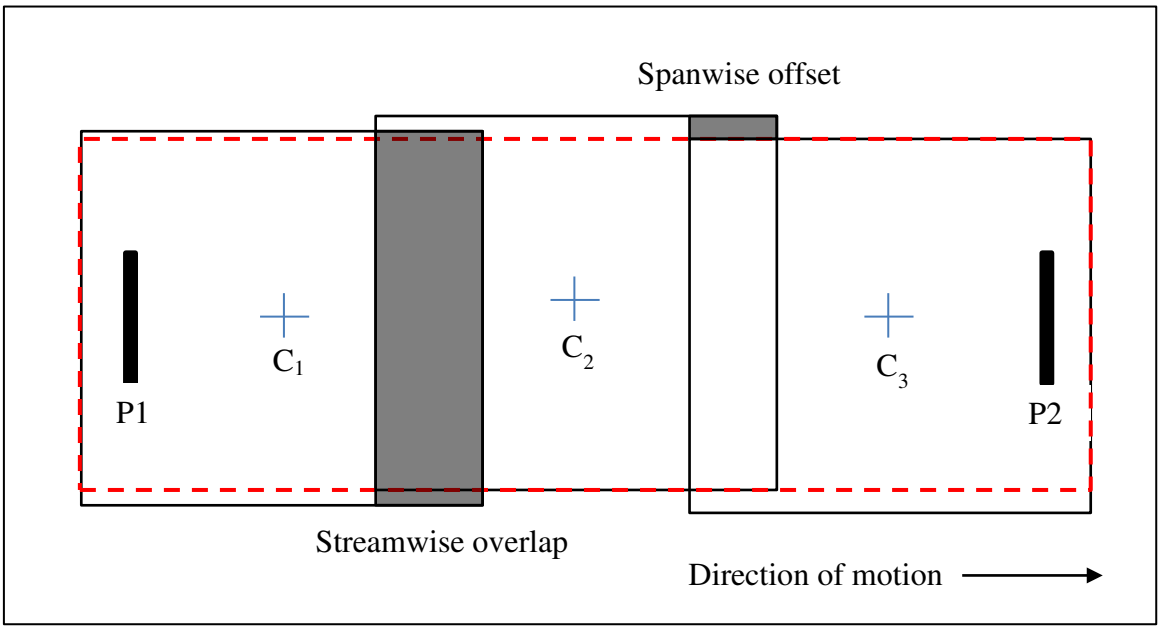

Fig. B1. Fields of view for the three sections.

ii. The computed velocity fields were then aligned in the streamwise and the spanwise directions using these reference points which gives the entire field of view, as shown in Fig. B1. The resulting velocity field had an overlap and an offset in the streamwise and spanwise direction respectively.

iii. To align the images in time, the raw images stored in Davis were used. The image at which the plate coincides with the reference point was identified manually. The time at which this occurs was obtained by matching the coordinates of C with the path data. Similarly, the time instances for the other fields of view were obtained.

iv. Using these time instances, the three sets of data were aligned sequentially. This solved the temporal offset.

v. To solve the spatial overlap and offset, a new set of data points in the streamwise and the spanwise directions were created through interpolation.

vi. The velocity fields were then interpolated to this new set of data points. This interpolation removed the spatial offset. However, in the overlapping region two values existed for each data point. This was solved through averaging for each time instant.

vii. Thus, the velocity fields with the desired field of view were obtained as a function of time.